Comparison of K-doped and pure cold-rolled tungsten sheets: As-rolled condition and recrystallization behaviour after isochronal annealing at different temperatures

Philipp Lied[a,], Carsten Bonnekoh[a], Wolfgang Pantleon[b], Markus Stricker[c,d], Andreas Hoffmann[e], Jens Reiser[a]*

a) Karlsruhe Institute of Technology, Institute for Applied Materials – Applied Materials Physics, 76344 Eggenstein-Leopoldshafen, Germany
b) Technical University of Denmark, Department of Mechanical Engineering, Section of Materials and Surface Engineering, 2800 Kongens Lyngby, Denmark
c) Institute of Mechanical Engineering, École Polytechnique Fédérale de Lausanne, CH-1015, Vaud, Switzerland
d) Karlsruhe Institute of Technology, Institute for Applied Materials – Computational Materials Science, 76131 Karlsruhe, Germany
e) PLANSEE SE, 6600 Reutte, Austria

Corresponding author:

*) Philipp Lied, Karlsruhe Institute of Technology, Institute for Applied Materials – Applied Materials Physics, 76344 Eggenstein-Leopoldshafen, Germany, Phone: +49 721 608 24093, E-Mail: philipp.lied@kit.edu

Preprint version (May 2019). Published in International Journal of Refractory Metals and Hard Materials, DOI: 10.1016/j.ijrmhm.2019.105047.

Abstract

Severely deformed cold-rolled tungsten is a promising structural material for future fusion reactor applications due to high melting temperature and excellent mechanical properties. However, the fine-grained microstructure after deformation is not stable at temperatures above 800 °C, leading to brittle material behaviour.

In this study, we utilize potassium-doping to inhibit recrystallization of tungsten sheets, a mechanism well known from incandescent lamp wires. We produced K-doped tungsten sheets by warm-rolling and subsequent cold-rolling with five different logarithmic strains up to 4.6, and equivalently rolled pure tungsten sheets. Both sets of materials are compared using EBSD and microhardness testing.

In both materials, the hardness increases and the grain size along normal direction decreases with strain; the densities of both, low and high angle boundaries, increase in particular during cold-rolling. The K-doped W sheet reaches the highest hardness with 772±8 HV0.1, compared to the pure W sheet with 711±14 HV0.1. All boundaries taken into account, a Hall-Petch relation describes the hardness evolution nicely, except a deviation of the K-doped tungsten sheet rolled to highest strain with its much higher hardness.

The similar structural and mechanical properties of both materials in the as-rolled condition allow further studies of recrystallization behaviour of the new K-doped material with a benchmark against the equivalent pure tungsten sheets. Isochronal annealing for 1 h was performed at different temperatures between 700 °C and 2200 °C. A sharp decrease in hardness to intermediate values is observed at around 900 °C for both materials, presumably reflecting extended recovery. A second decrease is observed at 1400 °C for pure tungsten, approaching the hardness of a single crystal and indicating recrystallization and severe growth of grains. For K-doped tungsten, however, the occurrence of the second decrease is shifted to higher temperatures from 1400 °C to 1800 °C with increasing strain and an intermediate hardness is maintained up to 1800 °C. We refer this dependence of the recrystallization resistance on strain in the K-doped material to the dispersion of K-bubbles, resulting in increased Zener pinning forces retarding boundary motion.

1 Introduction

The use of tungsten (W) and tungsten based materials in future fusion power reactors has been investigated and discussed for several years now [1]. Tungsten possesses the highest melting point among all metals (T_m = 3693 K [2]), therefore a low vapour pressure in the plasma, high wear resistance, as well as good high-temperature strength and good thermal conductivity. One major drawback of conventionally produced tungsten is its brittleness at room temperature, which

impedes the commercial use as structural material. Tungsten has therefore only been used as functional material [3]. However, this drawback can be overcome by cold working.

Recently, several authors reported astonishing mechanical properties of severely cold-rolled tungsten sheets. Wei and Kecskes [4] reported the effect of cold-rolling on the tensile behaviour of technically pure tungsten. Their results show that a decrease in rolling temperature from 800 °C to 400 °C results in an increase of the total elongation to fracture. The results by Wei and Kecskes have been recently been confirmed by Bonk et al. [5] and Reiser et al. [6].

Nikolic et al. [7] reported the fracture behaviour of cold-rolled tungsten sheets. Their results show significant higher values of fracture toughness compared to less deformed tungsten products of technical purity (>99.97 wt.%). Furthermore, the brittle-to-ductile transition temperature (BDTT) was found to be at room temperature. The results by Nikolic et al. have been recently confirmed and outperformed by Bonnekoh et al. [8]. Bonnekoh et al. produced five tungsten sheets (technical purity of >99.97 wt.% as well) rolled out from one and the same sintered ingot by various levels. Their results show that the transition temperature decreases with increasing degree of deformation and that the most severely cold-rolled tungsten sheet possesses a BDTT of −65°C. This demonstration of a tungsten material with a BDTT below 0 °C produced by severe cold-rolling could open a new era of the commercial exploitation and application of tungsten.

However, severely cold-rolled tungsten sheets have two major drawbacks: First, in most cases the heavily cold-rolled sheets are rolled down to very thin thicknesses in the range of e.g. 500 µm down to 50 µm. In most cases, such dimensions are of no use for structural applications. This drawback can be overcome by either using thicker sintered ingots, which allow to start the cold-rolling process at higher thicknesses (top-down approach), or by taking several thin cold-rolled tungsten sheets, stacking them together and bonding them into a thicker bulk material (top-down-bottom-up approach) [9].

The second drawback of cold-rolled tungsten sheets is their reduced temperature for the onset of recrystallization within a specific time period. It is well established that plastic deformation (especially cold working) leads to an increase of the internal stored energy. This increase in stored energy is caused by a deformation-induced increase in lattice defects and results in an increased driving force for recrystallization and hence a decreased recrystallization onset temperature. For example, for less deformed tungsten, static recrystallization starts after annealing for 1 h at about 1250 °C (1523 K) [3,10,11], whereas the most heavily cold-rolled tungsten sheets produced by Bonnekoh et al. show first signs of grain coarsening already after a heat treatment of 6 min at the much lower temperature of 1027 °C (1300 K) [12]. Therefore, in order to achieve a high-performance tungsten product, it is mandatory to stabilise the deformation microstructure.

Figure 1 summarises the facts presented above: cold-rolling decreases the BDTT significantly. However, this decrease is accompanied by a deterioration in the resistance against recrystallization. The question is whether it is possible to combine the improved low temperature fracture toughness of heavily cold-rolled tungsten sheets with increased recrystallization resistance, hence receiving a high-performance tungsten material for the use in extreme environments.

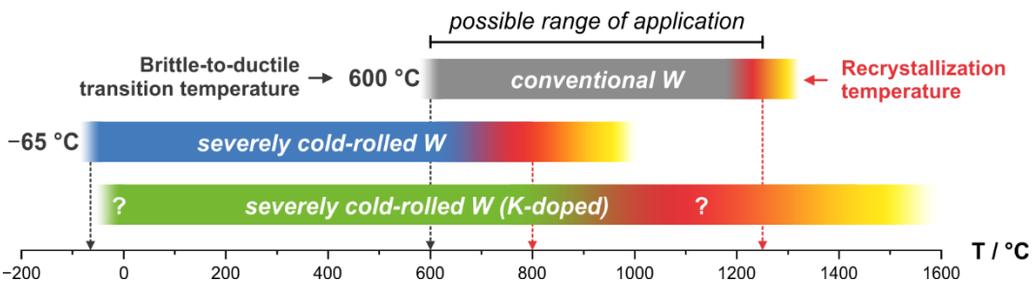

Figure 1. Conventional, coarse-grained tungsten possesses a BDTT of about 600 °C [8] combined with a static recrystallization onset temperature of about 1250 °C [3,10,11] (first row). By severe cold-rolling, the BDTT can be significantly decreased by more than 600 K down to −65 °C [8], however the deformation structure is unstable at temperatures above 800 °C (second row). By using a K-doped tungsten material, the recrystallization resistance might be increased while retaining a low BDTT, allowing the application as structural material in a wider temperature range (third row).

Our general material development strategy includes three steps: First, tungsten sheets are produced by applying high degrees of deformation at very low homologous temperatures [5,6,8,13]. Second, we will produce a bulk material by diffusion bonding of several layers of heavily cold-rolled tungsten sheets [9,14,15]. Third, we will use tungsten sheets with a microstructure that is stabilised against thermal influences. The latter is assessed in this study.

The stabilisation of an ultrafine-grained, severely deformed microstructure could be realised for example by formation of a solid solution [16], by adding second phase particles such as oxides [17,18] or carbides [19–21], as well as by doping with potassium (K) [22–25] (Table 1). The latter is what was chosen in our work.

Table 1. Strategies for the stabilisation of a heavily deformed microstructure against thermal loads.

Strategy	Examples	Comments	References
Solid solution	W-Mo W-Ta W-V	Materials were developed in order to decrease the BDTT	[16]
W matrix with dispersion of oxides	Cerium oxide (Ce_2O_3) Lanthanum oxide (La_2O_3)	Rare earth oxides; the formation of spherical particles from long, as-deformed ellipsoids follows the same mechanisms as described for AKS-doped tungsten	[17,18]
W matrix with dispersion of carbides	Tungsten carbides (WC, W_2C)	Introduction of WC particles into the matrix	[19]
	Zirconium carbide (ZrC)	RX temperature 100 K higher than pure tungsten	[20]
	Titanium carbide (TiC)	Material produced by powder injection moulding	[21]
	Hafnium carbide (HfC)	High thermodynamic stability; low solubility and diffusivity in tungsten at high temperatures	[3]
AKS-doping	Potassium (K)	Well established in lighting industry, content of few ppm	[22–24,26]

Stabilisation of the microstructure by doping with potassium is well established. During development of tungsten filaments for the lamp industry, an improved creep behaviour of filaments with impurities has been observed already in 1910. Systematic intentional doping of tungsten oxide powder was patented 1922 and the process has been refined by doping with aluminium-potassium-silicate at *Tungsram* in 1931. Therefore, K-doped tungsten is also referred to as AKS-tungsten (aluminium-potassium-silicate) or non-sag (NS) tungsten. Although these progresses were crucial for the development of early incandescent lamp wires, the role of K in stabilising the microstructure has been understood much later in the 1970th with support of modern tools of electron microscopy. There is very rich literature describing the processing of the material and the mechanisms that cause the increase of the recrystallization onset temperature and the improved creep performance ([22,23] and references therein). These mechanisms can be understood in the following context: Tungsten and potassium are mutually immiscible in the solid state and thus do not form any solid solution. During manufacturing, potassium is incorporated in a tungsten matrix as aqueous solution of potassium disilicate and aluminium nitrate or aluminium chloride. During sintering, the majority of these additives evaporates, but a partial quantity is retained due to formation of potassium aluminosilicates. In the further process, Al and Si are removed by diffusion and volatilisation and potassium partially remains in the sintered ingot, forming bubble structures [27]. During wire drawing, the K-bubbles are co-deformed with the tungsten matrix into long ellipsoids. During intermediate temperature treatments, these ellipsoids break up into rows of bubbles, following the mechanism of the Plateau-Rayleigh instability [23,28,29]. The formation of rows of bubbles from elongated ellipsoids is the result of the tendency of minimizing surface energy under the given restriction of material transport, a phenomenon also observed e.g. for La_2O_3 in molybdenum [18]. With increasing temperature e.g. during high temperature treatments, the physical state of potassium changes from solid to liquid and gaseous potassium (Table 2) and the vapour pressure in the K-filled bubble increases in equilibrium with the opposing Laplace pressure of the surface tension of the solid tungsten. Such pressurized K-bubbles can act as pinning points for dislocations and dislocation networks and form very strong barriers against subgrain and grain boundary migration [23].

Table 2. Basic thermodynamic data for potassium.

Properties	Potassium (K)
Crystal structure	bcc
Melting temperature (T_m)	63.71 °C (336.86 K) [2]
Boiling temperature (T_b)	767 °C (1040 K) [2]
Critical point (T_{crit}; p_{crit})	1925±30 °C (2198 K); 15.5±1.5 MPa [30]

Doping with potassium has been proven very successful for drawn wires. The question is whether and to what extend this technology can be transferred to rolled plates [31–33]. In order to answer this question and to elucidate the recrystallization mechanisms of K-doped tungsten plates, we produced five sheets that have been rolled out from one and the same sintered ingot to various degrees of deformation, representing logarithmic strains in the range of 1.6 to 4.6. The results are benchmarked against the results of pure tungsten sheets that have also been rolled out from one and the same sintered ingot by nearly the same logarithmic strains. In this paper we present the first results of this systematic study and provide answers to the following main questions:

1. How do the microstructure, texture and hardness develop during the process of severe warm and cold-rolling of K-doped tungsten sheets and its pure tungsten counterpart?
2. Can K-bubbles be detected and characterized by means of transmission electron microscopy (TEM)?
3. What dislocation features can be revealed by TEM investigations?
4. Do isochronal annealing experiments for 1 h give indications towards an improved recrystallization behaviour of heavily cold-rolled K-doped tungsten sheets compared to their pure tungsten counterparts?

This paper is organised as follows: First, in the “Background” section, we recall the main findings of two systematic studies on the deformation and fracture behaviour of heavily cold-rolled tungsten sheets. Afterwards, in the “Materials and methods” section, we describe the material production and give results of the chemical analysis. The “Results and discussion” section is divided into two parts: First, an in-depth characterisation of pure and K-doped W foils is presented to compare the as-rolled condition of both materials. This comparison includes a microstructural analysis by EBSD, further analysis of grain size and grain boundary disorientation distribution, texture components, TEM-imaging of K-bubbles and dislocation features with modelling of discrete dislocation dynamics, as well as hardness analysis by microindentation. In the second part, results of isochronal annealing experiments are shown to gain a first impression of the recrystallization resistance of K-doped W compared to pure W. This includes hardness analysis and backscattered electron (BSE) imaging in SEM. The findings are finally summarized.

2 Background: Systematic studies using rolled tungsten sheets

The current study on the recovery and recrystallization behaviour of K-doped cold-rolled tungsten sheets is in line with two other systematic studies performed by Bonk et al. [5,13] and Bonnekoh et al. [8]. Both studies investigated tungsten sheets, rolled out from one and the same sintered ingot, by various levels of logarithmic strain in the range of 1.8 to 4.1 (this equals engineering strains from 83% to 98%), and assessed the rolling induced evolution of the deformation structure and the fracture mechanisms. The main outcome of these studies will be described next.

The systematic study of Bonk et al. [5,13] assessed the mechanisms of plastic deformation of cold-rolled tungsten sheets. From their results, three main conclusions were drawn: First, the temperature dependence of the yield stress clearly indicates that bulk plasticity in heavily cold-rolled tungsten sheets is still controlled by the glide of screw dislocations, or more precisely, by the kink pair nucleation process. Second, all cold-rolled tungsten sheets possess a certain tensile ductility at room temperature. And third, the uniform elongation (ε_u) increases after heavy cold-rolling. The latter behaviour is astonishing as it violates the common relation between strength and ductility. In general, an increase in strength by dislocation hardening (Taylor, $\sigma_y \sim \rho^{0.5}$, where σ_y is the yield stress and ρ is the dislocation density) or grain boundary strengthening (Hall-Petch, $\sigma_y \sim d^{-0.5}$, where d is the mean grain size viz. mean free path for dislocation glide) is accompanied by a decrease of the uniform elongation.

Bonnekoh et al. assessed the mechanisms controlling the brittle-to-ductile transition (BDT) in pre-deformed, textured, polycrystalline tungsten [8]. The most heavily cold-rolled tungsten sheet produced by Bonnekoh et al. [8] possesses a transition temperature of −65 °C (208 K, loading rate of 1±0.1 MPa(m)$^{0.5}$ 1/s, single edge cracked tension specimen (SECT), crack introduced by spark erosion, samples loaded in mode I). The results by Bonnekoh et al. give hints about the evolving tensile ductility at room temperature of cold-worked tungsten. The results also indicate that the BDT is still controlled by the glide of screw dislocations and that the transition temperature decreases with decreasing spacing (λ) of dislocation sources along the crack front. Sources for dislocations may be the intersection points of grain boundaries with the crack front or dislocation multiplication processes such as the expansion of open or closed loops.

These studies give insight into the deformation and fracture mechanisms of severely cold-rolled tungsten sheets. It can be anticipated that heavy cold-rolling also results in a change of recovery and recrystallization mechanisms which will be assessed within this ongoing study.

3 Materials and methods

3.1 Materials

3.1.1 Rolling process

For this study, we produced two sintered ingots at PLANSEE SE (Reutte, Austria): (i) K-doped tungsten, which is commercially available as “WVM” with a K content of 60 ppm, (ii) technically pure tungsten (> 99.97 wt.% W), also commercially available. The abbreviations for both materials used in this study are W_K and W_{pure} respectively.

The rolling process at PLANSEE SE involved three steps, beginning with hot-rolling above the standard recrystallization temperature of 1250 °C to shape the ingot to a 5 mm thick sheet. The subsequent warm-rolling was performed at temperatures between 800 °C and 1000 °C with intermediate preheating steps. After a thickness reduction of around 80% (log. strain of 1.6), one part of the resulting sheet was separated as first sheet $W_K(1.6)$ of the series. The warm-rolling process continued and the sheets $W_K(2.7)$ and $W_K(3.1)$ at log. strains of 2.7 and 3.1 were separated likewise. In the last production step, the rolling temperature was reduced drastically below 300 °C (cold-rolling) and $W_K(3.7)$ as well as $W_K(4.6)$ were produced. In this way, we created W_K sheets with five different degrees of deformation and the same chemical composition. The same method was applied to W_{pure}, to create sheets with comparable log. strain ($\varepsilon_{\log}$) with $W_{pure}(1.6)$, $W_{pure}(2.7)$, $W_{pure}(3.3)$, $W_{pure}(3.7)$ and $W_{pure}(4.7)$. An overview and comparison of the resulting thicknesses and the equivalent engineering strain ($\varepsilon_{\mathrm{eng}}$) is given in Table 3.

Table 3. Comparison of initial hot-rolled plate (HR) and of investigated warm-rolled (WR) and cold-rolled (CR) W sheets by thickness (t), engineering and logarithmic strain (ε).

Material	rolling	t / mm	$\varepsilon_{\mathrm{eng}}$ / %	$\varepsilon_{\log}$ / -
W, K-doped	HR	5.0	0.0	0.0
W, K-doped	WR	1.03	79.4	1.6
W, K-doped	WR	0.35	93.0	2.7
W, K-doped	WR	0.22	95.6	3.1
W, K-doped	CR	0.127	97.5	3.7
W, K-doped	CR	0.052	99.0	4.6
W, pure	HR	5.4	0.0	0.0
W, pure	WR	1.09	79.8	1.6
W, pure	WR	0.36	93.3	2.7
W, pure	WR	0.19	96.5	3.3
W, pure	CR	0.134	97.5	3.7
W, pure	CR	0.051	99.1	4.7

3.1.2 Chemical analysis

To check the K content of W_K, including the content of relevant elements during the sintering process, and to compare it with W_{pure}, a chemical analysis of O, Al, Si and K contents was performed. Carrier gas hot extraction (CGHE) was used for O analysis, graphite furnace atomic absorption spectroscopy (GFAAS) for Si analysis and inductively coupled plasma optical emission spectrometry (ICP-OES) for Al and K analysis. Table 4 presents the resulting concentrations, which are well within the manufacturer's specifications limits [35,36].

Table 4. Chemical composition of both investigated materials. All values are given in ppm (by weight) with detection limit, arithmetic mean and standard deviation (SD). *) O and Al concentrations measured at KIT, IAM-AWP (three samples). **) Si and K concentrations measured at PLANSEE SE (two samples). Sum calculated as sum of the measured elements reported here (O, Al, Si, K).

		W, K-doped		W, pure		
Element	Det. limit	Mean	/ SD	Mean	/ SD	Method
O	3	5	±2	6	±2	CGHE*
Al	0.8	17.7	±0.1	1.40	±0.03	ICP-OES*
Si	5	5		<5		GF-AAS**
K	5	60.0	±0.5	<5		ICP-OES**

3.1.3 Annealing

Isothermal temperature treatments between 700 °C up to 1200 °C were done at KIT with a Nabertherm LHT 08/18 furnace, while temperature treatments from 1400 °C up to 2200 °C were done at PLANSEE SE in hydrogen atmosphere. Except the samples for the hydrogen furnace, samples of each W sheet were encapsulated in evacuated quartz glass ampoules to prevent oxidation in the Nabertherm furnace. Each ampoule contained five sheets of the same material (W_{pure} or W_K) all with different thicknesses. Ampoules with W_{pure} and W_K were annealed simultaneously to guarantee the same temperature treatment.

3.2 EBSD measurement

Electron backscatter diffraction (EBSD) has been performed on polished cross sections containing the rolling direction (RD) and normal direction (ND) of the W sheets. This surface has been prepared by grinding, polishing and subsequent electropolishing with aqueous NaOH solution. Analysis of the W microstructure was performed by using a Zeiss Merlin field-emission-gun scanning electron microscope (SEM) equipped with an EDAX Hikari high-speed EBSD camera. The SEM acceleration voltage was set to 20 kV with a probe current of 10 nA. Data has been acquired as hexagonal pixel pattern. An EBSD step size of 40 nm has been chosen, as a compromise between reasonable scan durations with sufficient large map sizes (40x40 μm^2) and the ability to detect grain sizes as small as possible but also large, recrystallized grains. Choosing a lower step size leads to an enhanced uncertainty like SEM probe current and/or stage instabilities and much longer scan durations. For overview orientation maps of thick tungsten sheets, a step size of 200 nm has been chosen.

Data evaluation was performed with EDAX OIM Analysis™ v7.3.1. Data points below a confidence index of 0.1 were removed during post processing. Except a grain CI standardisation, no clean-up of the data was executed and the orientation of the data points remained unchanged. Boundaries with disorientations above 15° between neighbouring pixels are defined as high angle boundaries (HABs) [37], while boundaries between 2°-15° are considered as low angle boundaries (LABs). Orientation distribution functions (ODF) are calculcated as harmonic series expansion up to rank 34.

3.3 TEM investigations

Samples for transmission electron microscopy (TEM) were prepared as discs with 3 mm diameter by punching, then using a TENUPOL device for electropolishing with aqueous NaOH solution as electrolyte at room temperature. For TEM examination a FEI Tecnai 20 FEG microscope was used with an acceleration voltage of 200 kV, a scanning unit for scanning TEM (STEM) with a high-angle annular dark field (HAADF) detector, and an EDX detector for elemental analysis.

3.4 Microhardness measurement

For Vickers hardness measurements, a Clemex CMT.HD indenter has been used with a test load of 0.9807 N (100 g, HV0.1). The hardness indentation was performed at the polished faces of embedded foils on the RD/ND plane (i.e. along transversal direction). At least seven points in different areas of every sample have been measured for calculation of arithmetic mean and standard deviation of the distribution. The size of the hardness indents in the specimen are in the range up to 25 µm. While the thickness in the transversal plane is still large enough for the 127 µm to 134 µm thick sheets to be in conformity with the standards of DIN EN ISO 6507-1 [38], the thickness of the ~50 µm sheets is not enough so that a hardness indent would have the required distance of 2.5 times the diagonal of the indent to the border of the sheet. However, if this would have an influence on the measurement, it would lead to lower HV values. As seen in the correlation of hardness to grain size later on, this is clearly not the case as the values are following the trend of the thicker sheets (for W_{pure}) or are even higher in hardness (for W_K).

3.5 Modelling dislocation interaction by discrete dislocation dynamics (DDD)

For the modelling of frequently observed dislocation features such as e.g. junctions, a three-dimensional discrete dislocation dynamic (DDD) code developed by Weygand et al. [39] was used. DDD is a method where dislocations are discretized as piecewise linear segments and their motion is described based on the externally applied load and the elastic interaction between dislocations. Mechanisms such as cross-slip and the formation of junction segments are included through constitutive laws.

4 Results and discussion

4.1 As-rolled condition

4.1.1 Microstructural analysis

For analysing the orientation of the grains in cold-rolled tungsten sheets, we performed EBSD analysis for pure and K-doped W for all five sheets of different thickness respectively. Because preliminary studies already investigated normal (ND), rolling (RD) and transversal viewing direction (TD) of cold-rolled tungsten sheets [5], we concentrated our study on investigating the RD/ND section. This section reveals the most striking microstructural features of rolled metal sheets such as elongated grains along RD and grain size reduction along ND with increasing degree of deformation. As expected, resulting orientation and boundary maps clearly reveal these features (Figure 2). For instance, sheets with lower strain (up to $\varepsilon_{\log}$ = 3.3) still maintain grains not extending more than 5 µm along RD. With increasing strain, the grains become more and more elongated and gradually develop a pancake like shape, which has been described in previous studies [5,40]. Because of grain size reduction along ND, more boundaries can be seen in boundary maps of the same size for sheets with higher strain. With increasing strain, high angle boundaries (HABs) are apparently dominating. This can be seen especially in boundary maps of pure W (Figure 2, left). Interestingly, K-doped W shows a tendency to form several micron thick bands, containing large amounts of low angle boundaries (LABs) and consisting predominantly of a single orientation. Such “orientation bands” can still be found in the sheet with highest strain (Figure 2, orange markings on the right). In pure tungsten, on the contrary, HABs and LABs are distributed more homogeneously along ND. This could influence the subsequent recrystallization behaviour and could be of more importance in future studies.

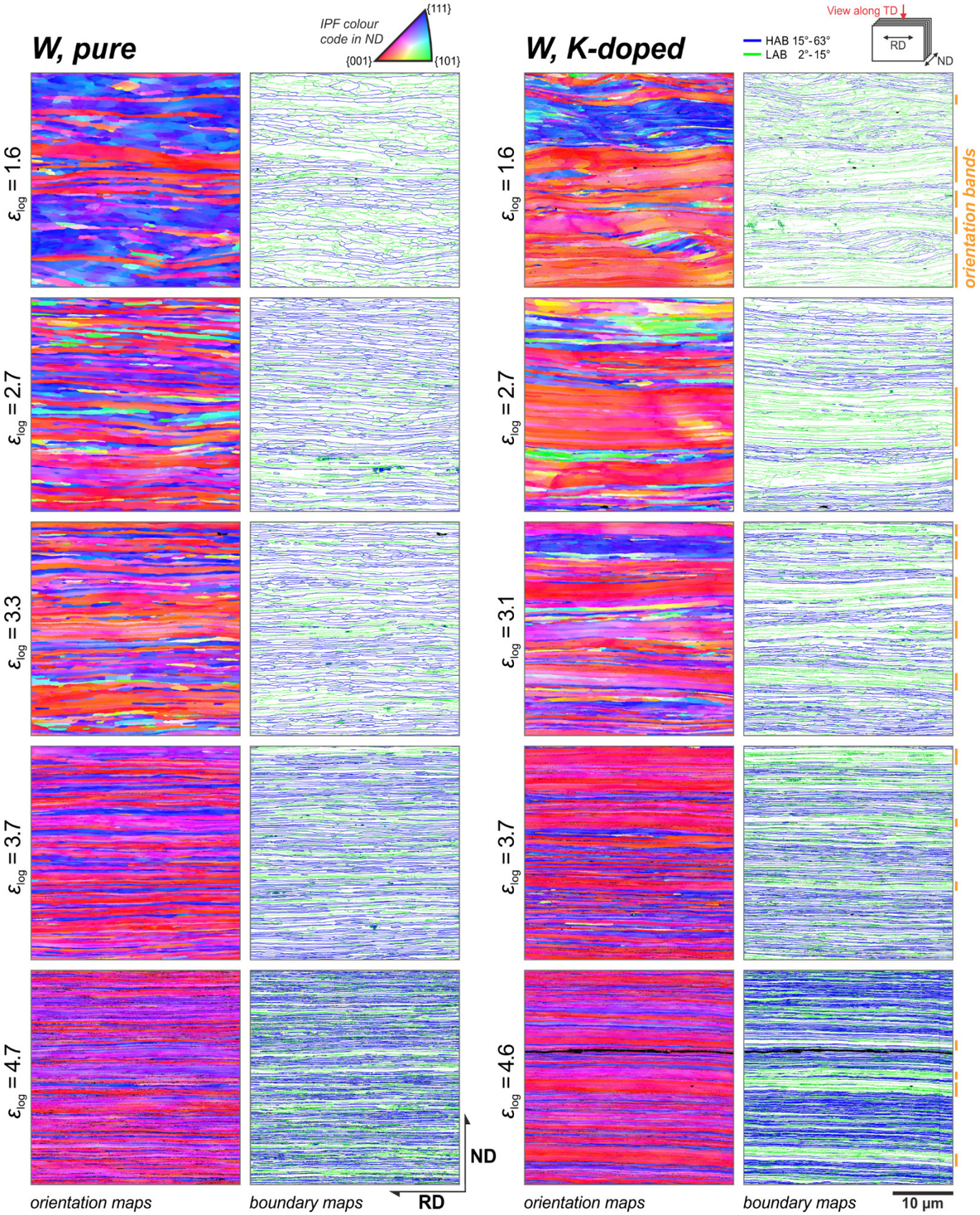

Figure 2. Orientation and boundary maps on RD/ND sections for technically pure W (left) and K-doped W (right) with five log. strains ($\varepsilon_{\log}$) respectively. In the orientation maps, the crystallographic direction along ND is represented by a colour according to the IPF placed above. In the boundary maps, high angle boundaries with disorientations above 15° are highlighted in blue, low angle boundaries with

disorientation angles between 2° and 15° in green. Pixel with low confidence index (<0.1) are drawn black. On the right, orientation bands observed in W_K are highlighted by orange bars.

4.1.2 Grain size

The grain size along ND (or chord length) is determined by measuring the length between line intercepts with HABs along ND. This was done for all investigated W sheets, the resulting grain size distributions are presented in Figure 3 (Note that in this manner only multiples of the EBSD step size of 40 nm are determined as grain sizes). The fraction of smaller grain sizes is growing with increasing strain for both materials. The grain size distribution follows a lognormal probability density function curve $f(d)$ which is defined as

$$f(d) = \frac{A}{\sqrt{2\pi}\,\sigma\,d} \cdot exp\left(\frac{-(ln(d/\mu))^2}{2\sigma^2}\right) \quad (1)$$

with A as normalisation factor (necessary due to the missing grains below 40 nm), μ as mean and σ as standard deviation. The lognormal distribution is a skewed curve with a steep slope towards lower grain sizes. Such a lognormal distribution is known for grain size distributions in many polycrystalline materials and has been shown for cold-rolled tungsten sheets as well [41]. The probability density function has been fitted for every W sheet in this study. While reasonably fitting is achieved for sheets with $\varepsilon_{\log} \leq 3.7$, especially the presented distribution for $W_K(4.6)$ shows its maximal relative frequency at the smallest bin of 40 nm and the decrease towards zero cannot be observed. This is due to the very fine grain size in this sheet, which just cannot be resolved by the chosen EBSD step size of 40 nm (Figure 3). Yet, this resolution limit is not an issue for sheets with $\varepsilon_{\log} \leq 3.7$, because the maximum relative frequency of the grain size distribution is observed at 80 nm or even 120 nm. The relative frequencies at smaller sizes are lower and fit the lognormal distribution satisfactorily. This is also still true for the $W_{pure}(4.7)$ grain size distribution presented here (Figure 3b) and also for most of the other mappings of $W_K(4.6)$ (not shown here).

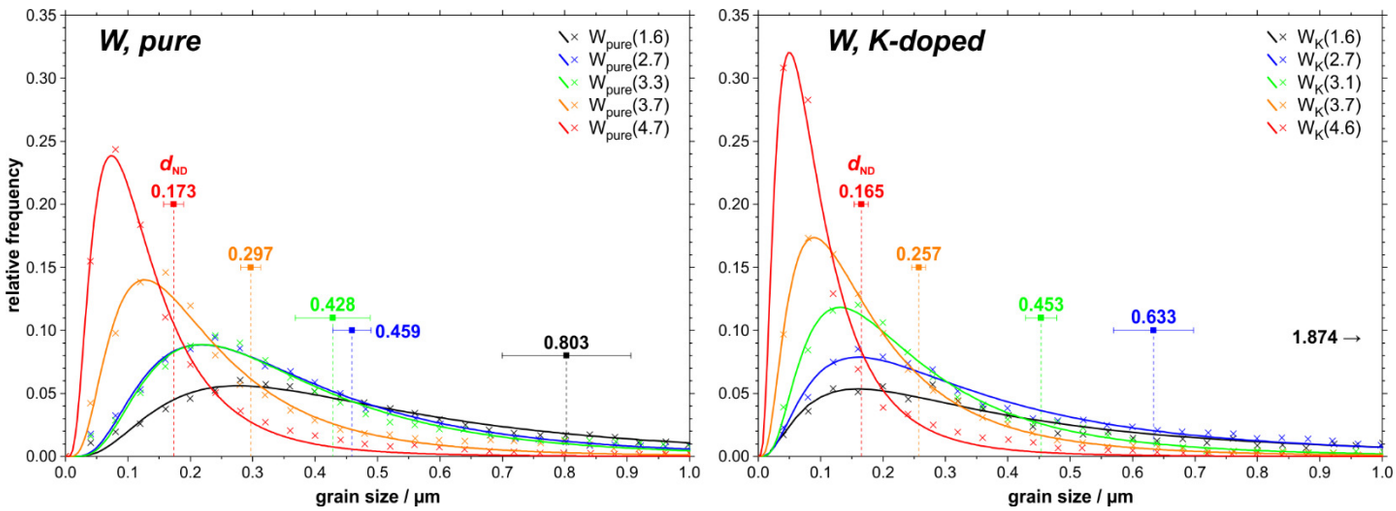

Figure 3. Grain size distribution (measured by intercept length along normal direction) of pure and K-doped W with lognormal fitting curve. Relative frequencies are deduced from boundary maps shown in Figure 2. Arithmetic mean (d_{ND}) and standard deviation are derived from three boundary maps for each sampled W sheet (also shown in Figure 4).

To evaluate this effect of EBSD step size on grain size distribution, we performed additional mappings on W_K in the same sample area with 20 nm. For the sample with $\varepsilon_{\log}$ = 3.7, the determined average grain size is 2% smaller for the 20 nm mapping compared to 40 nm mapping. For the sample with $\varepsilon_{\log}$ = 4.6, the average grain size is 10% smaller for the 20 nm mapping compared to 40 nm mapping. Therefore, one has to keep in mind that the real average grain size of sheets with highest strain could be slightly smaller than deduced from EBSD with a step size of 40 nm. However, the reasons already mentioned to maintain this measuring method are still valid: Because our study aims to investigate the recrystallization behaviour and much larger grain sizes need to be investigated, a common step size is preferred, allowing a direct comparison of maps of as-rolled and annealed samples.

A clear trend can be recognised: Higher strain leads to finer grain sizes in ND. To substantiate the finding, three maps have been acquired for each condition at different distance from the sheet surface. For each map, the average grain size ($\overline{d_{ND}}$) has been calculated as arithmetic mean of the measured grain sizes. From the average grain sizes of the three corresponding maps, mean values (d_{ND}) and standard deviation (SD) are calculated and presented in Figure 4. A high SD indicates heterogeneity in the sample.

If only HABs (>15°) are considered in determining the grain size as above, the results show consistent grain sizes for W_{pure}, also compared to other studies with pure W sheets [5,41]. W_K(1.6) shows very different values for the different areas (high SD, note the logarithmic scale) and much coarser grains sizes with 1.87 µm than its counterpart W_{pure}(1.6) with 0.80 µm. This difference between W_K and W_{pure} is reduced in the next rolling step. During further rolling, W_K-sheets show a more pronounced grain size reduction than W_{pure}. This results in slightly smaller grain sizes in the last two rolling steps (CR). However, concluding that K-doping would be beneficial for grain size reduction is premature, because during warm-rolling of W_{pure}, between ε_{log} = 2.7 to ε_{log} = 3.3 no grain size reduction is achieved (see also Figure 3). This behaviour (which did not occur for W_K) might be attributed to either dynamic restoration during the rolling pass or some static restoration during intermediate annealing (at temperatures <1000 °C) between the passes. Fine-grained pure W sheets are presumed to be more prone to recovery and recrystallization than their K-doped counterparts. This might be the reason why W_K sheets with ε_{log} ≥ 3.1 show a slightly more prominent grain size reduction than W_{pure}. Nonetheless, after CR treatment both materials achieve similar average grain sizes of down to 0.165 µm for W_K(4.6) and 0.173 µm for W_{pure}(4.7).

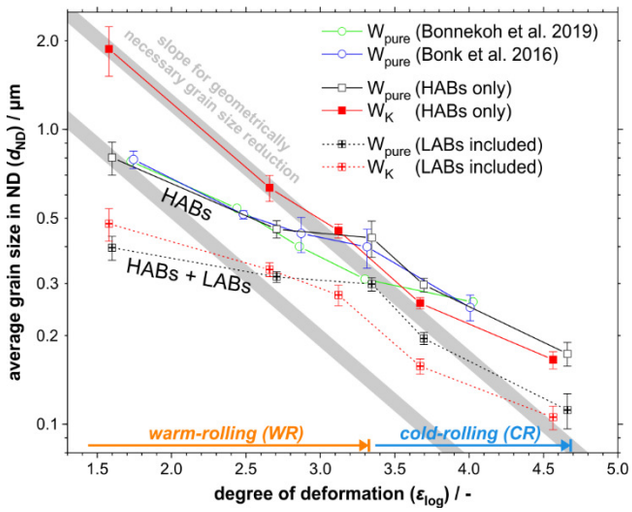

Figure 4. Average grain size (d_{ND}) along normal direction (see mean values in Figure 3) in dependence on the logarithmic strain of rolled W sheets. Mean values and standard deviation (with and without taking into account LABs) are derived from three grain boundary maps for each sampled sheet. For comparison, values from other studies have been added [5,41]. Note, that the grain size is shown on a logarithmic axis. A grey band indicates the theoretical grain size reduction, if the boundaries are following the imposed thickness reduction (meaning that by the line intercept method, one would count the same amount of boundaries along ND through the entire sheet thickness at any point of the grey line).

Taking into account only HABs, the grain size in W_K follows an exponential decrease with strain (seen as linear behaviour in Figure 4 due to the logarithmic axes) almost exactly as the evolution of the plate thickness (as shown by the grey band). Only for the largest strain of cold-rolling deviations are observed. This is a rare observation. Usually, grain size reduction occurs much slower than the thickness reduction, meaning that in summary grain boundaries are not multiplying but disappearing at larger strains [40]. It almost seems like the restriction of any HAB movement by the K bubbles enforces the HABs to follow the imposed thickness reduction (see grey band in Figure 4), meaning that the rate of grain boundary formation and annihilation would be equal. However, the reason for such behaviour might rather be a consequence of the relatively thick orientation bands, where neighbouring grains of similar orientation are separated by boundaries with low angles only (Figure 2). In an alternative approach, these LABs are accounted for as well and the boundary spacing between all types of boundaries are reported also in Figure 4. As seen from Figure 4, the spacing between all boundaries does not decrease in the same strong manner as the HABs and a more similar evolution is observed for both, the pure and K-doped sheets. Compared to the WR passes, grain size reduction during the CR passes is enhanced when taking into account all

boundaries (in case of HABs the grain size reduction in W_K becomes less during CR). Although grain size reduction is less pronounced during CR, up to a strain of 4.7 no evidence for saturation of the grain size reduction is observed, in contrast to abundant claims in literature (e.g. [42] and references therein). In this manner, an even stronger grain size reduction should be possible by further cold-rolling, although in practice macroscopic longitudinal cracking of the tungsten sheets during rolling at very high strain sets a certain limitation for further thickness reduction.

4.1.3 Grain boundaries and disorientation angles

The distribution of disorientation angles between pairs of indexed points in the orientation maps can be seen in Figure 5 where directly boundary densities are reported, i.e. the frequency of boundaries with certain disorientation angles in the orientation maps, divided by the number of indexed points. Distinct peaks are found in the disorientation angle distribution: A peak at 6.5°, which is attributed to deformation-induced boundaries, and two peaks near 54.7° and 60°, which increase after cold-rolling and will be explained while discussing the ODF below.

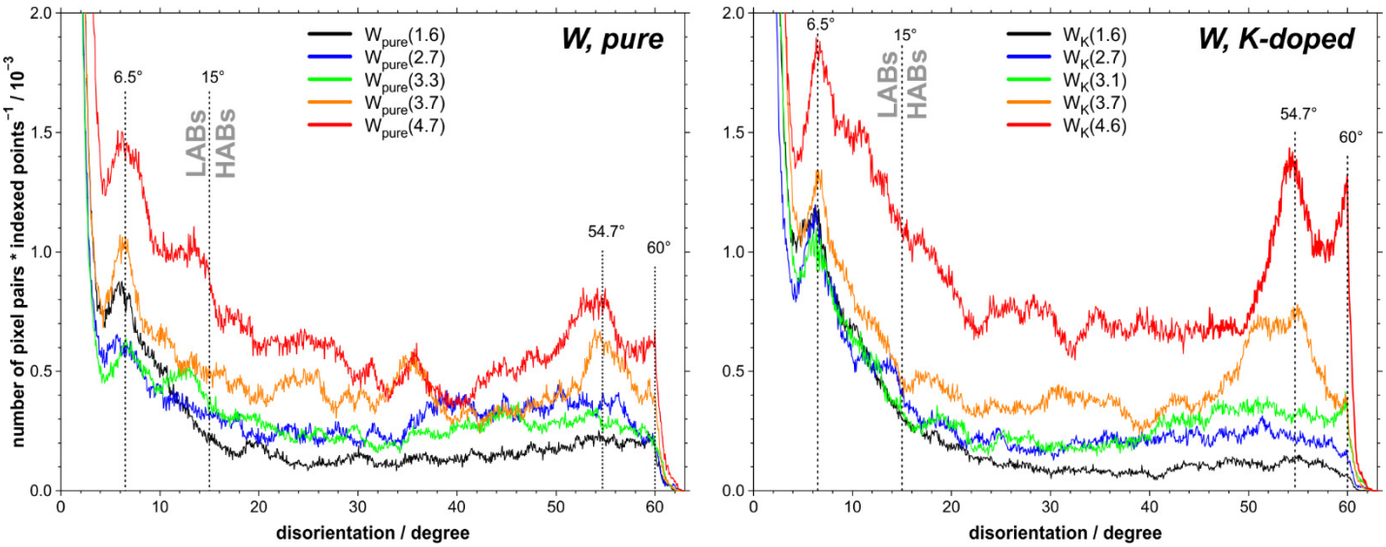

Figure 5. Disorientation angle distribution of number of pixel pairs with specific disorientation angle, normalised to total number of indexed pixel in the respective orientation map (i.e. boundary density). The disorientation angles of neighbouring pixel pairs are calculated from the orientation maps shown in Figure 2.

The following behaviour can be observed: As expected, the total density of grain boundaries increases with strain (see also Figure 2). Warm-rolling (WR) up to $\varepsilon_{\log}$ = 3.3 increases only the density of HABs, the density of LABs (<15°) is constant or even decreases in case of W_{pure}(2.7). Cold-rolling (CR) increases both, the density of HABs and as well LABs by a significant amount. This relation is also described in Figure 6, where the HAB and LAB length is summarised and normalised to the indexed area (area of all indexed hexagonal pixel) in the respective grain boundary map. The obtained boundary density depends on strain. The HAB density increases steadily during WR, but the rate is notably increasing during CR. As can be seen again, the density of LABs is increasing only during CR, not during WR. On the other hand, the ratio between increase of LAB and HAB density becomes constant during CR.

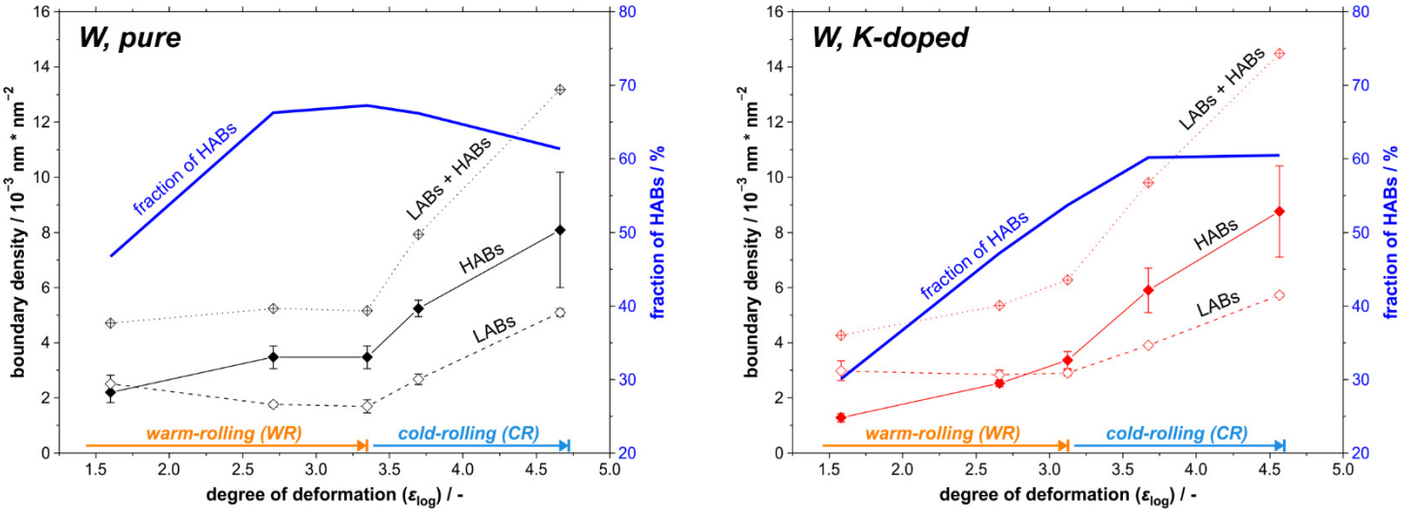

Figure 6. Boundary density for HABs (>15°) and LABs (2°-15°) in the respective boundary map, i.e. total boundary length normalised by indexed area, in dependence on strain. Mean values and standard deviation are derived from three grain boundary maps for each sampled W sheet. The respective ratio between HAB to LAB density is plotted in blue.

The reason for the constant or even *decreasing* density of LABs during WR can be seen in two processes. First, a transformation of existing LABs into HABs. Second, annihilation of LABs. As WR is conducted above 800 °C with warming up phases between the rolling passes, and hence the entire processing occurs above the knee temperature of tungsten, all dislocation types can glide without requiring thermal activation and therefore recovery mechanisms can take place. This can also be concluded from the microhardness data after isochronal annealing experiments shown in a later section, where restoration phenomena occur at 800 °C and above (Figure 15). Whether the process of annihilation or transformation to HABs is dominating the development of LABs during WR cannot be concluded with certainty.

The above discussion for WR raises the question why the LAB density is *increasing* strongly during CR. For the observed phenomenon, there are two main reasons: (1) Due to formation of preferred orientations, forming the rolling texture, the orientations of neighbouring grains may converge and initial HABs develop into LABs. Such a process might be indicated by the orientation bands observed especially in W_K. (2) While LABs are evolving into HABs, new incidental dislocation boundaries are constantly formed by mutual trapping of glide dislocations [43]. The formation rate of such dislocation boundaries should be rather independent of the rolling temperature. The antagonistic process of LAB annihilation by recovery processes, however, occurs at a much lower rate during CR compared to WR. This can be also inferred from Figure 4, where the decrease in grain size (considering all boundaries including LABs) is much more pronounced during CR than during WR, meaning that the annihilation rate is drastically decreased during CR. Taking into account, that the temperature during CR is below 300 °C, the annihilation should be governed solely by dynamic recovery. During the processing at higher temperatures above 800 °C, on the contrary, both, dynamic recovery during WR and static restoration between the WR passes should be active.

The investigation reveals that a production of tungsten material with high LAB density is only possible by rolling at lower temperatures than 800 °C. How the LAB density affects the hardness is shown in 4.1.5.

4.1.4 Texture

For each investigated sheet, the orientation distribution function (ODF) has been determined to give an impression of the rolling texture evolution during the processing steps (Figure 7). For the pure tungsten sheets, a defined rolling texture with pronounced γ-fibre ({111} in rolling plane) and α-fibre (<110> along RD) components can be recognized even at the lowest strain. During further processing, the {111}<121> orientations along the γ-fibre get more pronounced, while the density of the {001}<110> rotated cube orientation (as part of the α-fibre) is increasing with every rolling step. The maximum density of 56 multiples of a random density (MRD) at highest strain is shifted towards the {113}<110> orientation, which reflects a rotation around RD. In general, a rotated cube texture is commonly seen in other cold-rolled bcc metal sheets like ferritic steels (e.g. [44–46]) and has been shown for cold-rolled tungsten sheets as well [5,8,34]. It is also the reason for the

disorientation peak at 54.7° observed in Figure 5, since the pronounced {001}<110> rotated cube orientation is disoriented between 54.7° and 56.6° from the {111}<110> and the pronounced {111}<121> orientations on the γ-fibre, respectively. The peak at 60°, however, originates from components with <110> along RD in mutual twin relation. This is also indicated by the maximum peak for the α-fibre shifting towards {113}<110> orientation. The increase in orientation density, especially for the α-fibre, is a usual behaviour for plane strain rolling [47], however such high orientation densities for the thinnest sheet are exceptional and caused by the high rolling strain.

The K-doped material has a similar rolling texture development and reaches even higher orientation densities (up to 75 MRD) near the {001}<110> rotated cube orientation. Another difference in the ODFs is that for W_K(1.6) very distinctive peaks of the {111}<121> orientations in the γ-fibre are present, in contrary to its W_{pure}(1.6) counterpart (Figure 7). Since other ODF plots from different areas of the same sampled sheet (not shown here) do not show these features and are more similar to W_{pure}(1.6), the presented ODF section of W_K(1.6) is not considered representative. This discrepancy reveals certain heterogeneities of the crystallographic texture within the K-doped material at lowest strain, while the texture gets more homogeneous with increasing strain.

This heterogeneity has been scrutinized by extensive EBSD-mapping of the whole 1 mm-sheet-thickness along normal direction for both materials. The resulting orientation maps of W_{pure}(1.6) show a high fraction of α- and γ-fibre components in the centre of the sheet section, while towards the upper and lower surface other texture components like the copper {112}<111> and brass component {110}<112> prevail (Figure 8, orientation maps and ODFs). The latter orientations on the surface are known as part of a shear texture in bcc metals with a rotation relation of 90° to the rolling texture [48]. For ferritic steels processed by large strain rolling, it is well known that surface regions can develop a quite different texture than observed in the through-thickness centre regions of the sheet [49]. We suspect this behaviour occurs also in other bcc metals like tungsten.

W_K(1.6) reveals the same rolling and shear texture components as W_{pure}(1.6), but their distribution is more heterogeneous. The dominating α- and γ-fibre components in the centre are arranged in alternating bands with thicknesses up to 20 µm, solely containing LABs (Figure 2 and Figure 8). These orientations bands contain a single texture component. Especially bands consisting of γ-fibre, show additionally signs of shear banding (Figure 8, magnified areas 1 and 2). With increasing strain, the observable presence of shear bands decreases significantly. Especially for the thinnest sheet, no shear banding can be recognised and the distribution of texture components appears more even. Orientation bands of α-fibre still persist with a thickness of up to 2 µm along ND. In comparison, orientation bands are rare in the reference pure W sheet with a maximum thickness of 1 µm and the distribution of LABs and HABs is more even (Figure 2, W_K(4.6) and W_{pure}(4.7)). The reason for the heterogeneities in W_K are unknown, but as similar orientation bands have been found in preliminary investigations on comparably produced pure W sheets from PLANSEE SE (not shown here), this phenomenon is not restricted to K-doped W sheets. Whether these orientation bands of single texture component also influence the recrystallization behaviour, is a matter of further investigations.

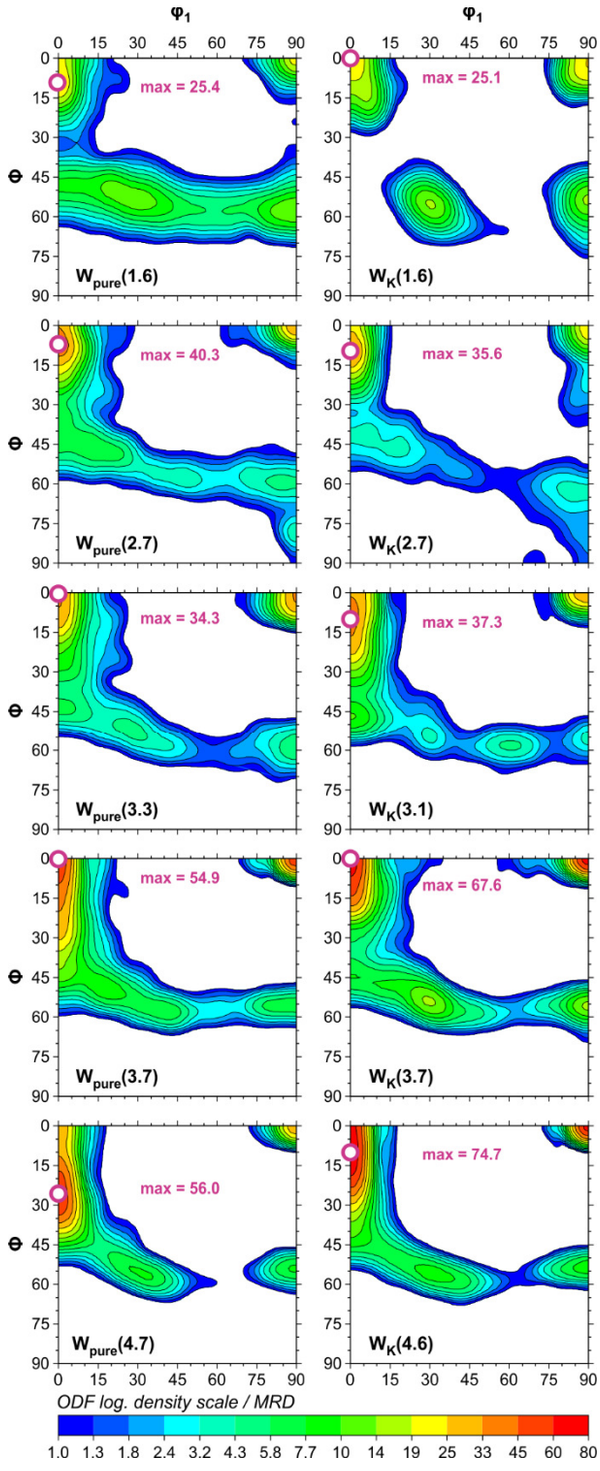

Figure 7. φ_2 = 45° sections of the orientation distribution functions (ODFs), describing the crystal orientation distribution in the Euler space for each investigated sheet (Bunge notation is used). Orientation densities are given in multiples of a random density (MRD), respective maxima are marked by a purple circle. The ODFs are deduced from the same data sets used for the orientation maps shown in Figure 2.

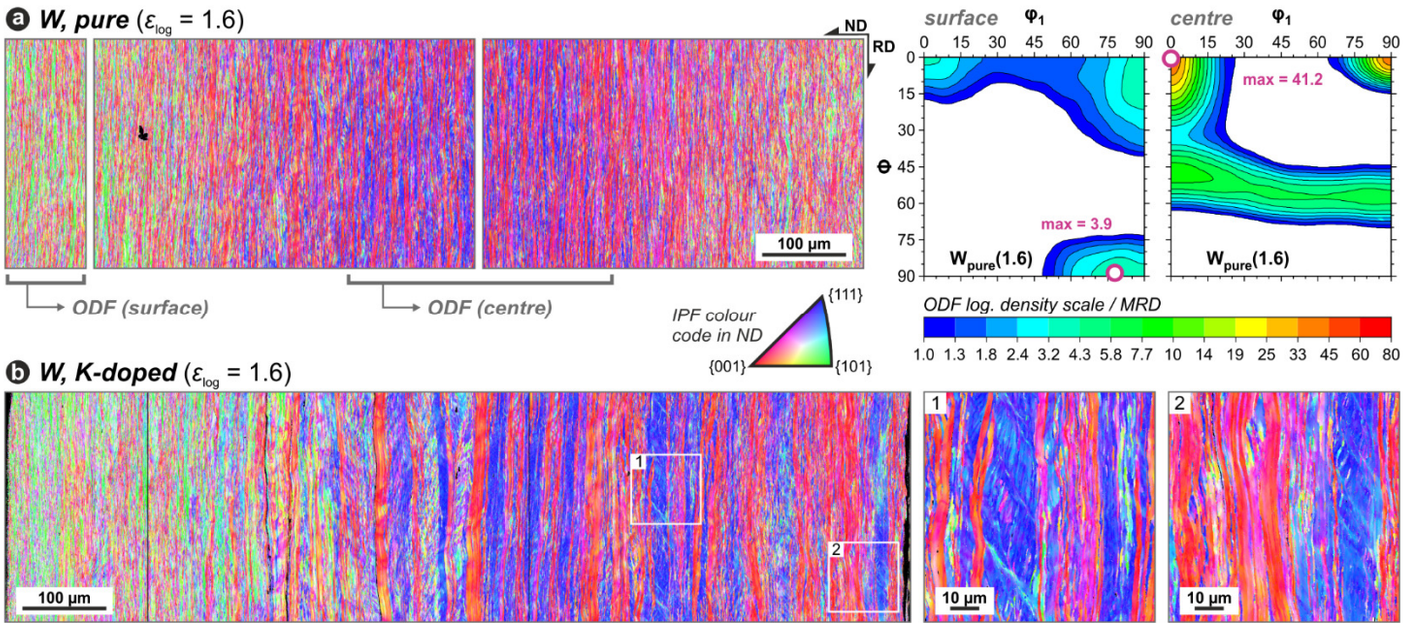

Figure 8. Orientation maps of whole thickness sections (RD/ND) for the 1 mm-sheets of (a) $W_{pure}(1.6)$ with calculated ODFs from marked areas on surface and centre and (b) $W_K(1.6)$ with magnified areas 1 and 2. Note the high amount of sigmoidal shaped shear bands in the K-doped material.

4.1.5 Microhardness and implications by Hall-Petch relation

Vickers microhardness measurements on the prepared RD/ND sections have been carried out as first evaluation of the mechanical properties of the different sheets. The results can be seen in Figure 9 in comparison with preceding studies for pure W, produced in a similar way by WR and CR at PLANSEE SE [5,8]. Starting at around 590 HV0.1 for both, $W_K(1.6)$ and $W_{pure}(1.6)$, the hardness increases by small amounts during WR up to ε_{log} = 3.3, but increases drastically by CR up to values of 711±14 HV0.1 for $W_{pure}(4.7)$ and 772±8 HV0.1 for $W_K(4.6)$. It seems that in contrary to preceding studies on pure W [5,8], the hardness development is mainly influenced by the CR process in both materials.

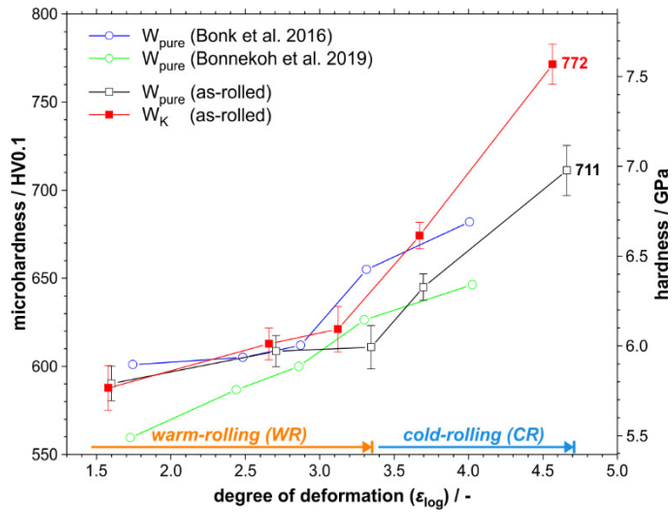

Figure 9. Vickers microhardness values of K-doped and pure W sheets in dependence to degree of deformation (log. strain). For comparison, values from other studies have been added [5,8].

Unfortunately, the comparison of hardness between W_K and W_{pure} in this study is complicated due to a slight variation in the hardness development: While the hardness gain is very similar for both materials between rolling steps ε_{log} = 1.6 and

$\varepsilon_{\log}$ = 2.7, the hardness remains nearly constant for W_{pure} in the next rolling step to $\varepsilon_{\log}$ = 3.3 (Figure 9), which is also reflected in the grain size showing no decrease in this interval (Figure 3), whereas the hardness of W_K increases further during WR to $\varepsilon_{\log}$ = 3.1. This difference, that W_K becomes harder than W_{pure} despite smaller strain increment, could be caused by temporal variations in the WR process, e.g. slightly longer warming up times of W_{pure} between the WR steps and resulting restoration processes. One can also argue that K-doping should lead to higher resistivity against restoration throughout the warming up steps below 1000 °C, gaining an advantage in hardness compared to W_{pure}. Additionally, the W_{pure} sheet received higher strain ($\varepsilon_{\log}$ = 3.3) than W_K ($\varepsilon_{\log}$ = 3.1) during WR. Regarding both effects of different hardness evolution and strain development, this could give W_K an advantageous starting point for the CR process, resulting finally in its higher hardness.

The general reason for the hardness increase can be seen in the grain size reduction (Figure 3, Figure 4) and the increasing grain boundary density (Figure 5, Figure 6). A Hall-Petch relation for the dependence of hardness to the grain size along ND (${d_{ND}}^{-1/2}$) is tested and the Hall-Petch coefficient k_1^* is calculated [50,51]. For the WR samples, a linear fitting curve applies very well (Figure 10a). However, an extrapolation of the linear fit is not able to describe the behaviour of the CR samples, where the hardness increases during CR considerably more than expected by the Hall-Petch relation in the WR regime. Thus, besides strengthening through high angle boundaries, additional effects have to be accounted for. The most obvious cause is strain hardening by the storage of dislocations, which is also indicated by the higher dislocation densities observed qualitatively in TEM investigations (presented in Figure 11). Secondly, an increasing LAB density is detected during CR (Figure 6). This leads to the question, which influence the high LAB density has on the hardness development.

In the literature, LABs are commonly not included in the Hall-Petch relation. Besides hardness, the relation has been used to describe the dependence of grain size on other mechanical properties as well, initially for the yield stress and later on also for the flow stress of polycrystalline metals and alloys [42,43,52]. It has been shown that at low to medium strains the Hall-Petch relation between grain size d_{HAB} and flow stress at a particular strain σ_f applies satisfactorily, if only HABs are considered. The strength is the sum of the contributions from the flow stress in the grain interior σ_0 and from the resistance to dislocation movement caused by the presence of grain boundaries with mean distance d_{HAB} with k_1 as a coefficient at given strain:

$$\sigma_f = \sigma_0 + k_1 \, {d_{HAB}}^{-1/2} \tag{2}$$

Hansen [43] discussed the additional contribution of LABs to the strengthening in tensile tests. It has been shown that for severely deformed metals with grain sizes in the submicron range, equation (2) becomes invalid and an additional contribution from dislocation boundaries has to be included. Based on an assumption of an additive strengthening from LABs and HABs, the flow stress might be expressed as

$$\sigma_f = \sigma_0 + M\alpha G\sqrt{1.5b(S_V\theta)_{LAB}} + k_1 \, {d_{HAB}}^{-1/2} \tag{3}$$

where M is the Taylor factor, α is a number, G is the shear modulus. The strengthening of LABs is attributed to their dislocation content $1.5b(S_V\theta)_{LAB}$ with b as Burgers vector, S_V as area of boundaries per unit volume and θ as misorientation angle. As an alternative approach (and valid only for severely deformed metals), a modified Hall-Petch relation is considered, where instead of the spacing between HABs the mean boundary spacing d_B is taken into account without discriminating between HAB and LAB:

$$\sigma_f = \sigma_0 + k_2 \, {d_B}^{-1/2} \tag{4}$$

This approach uses value k_2 as a constant, however it is unknown if the boundary properties depending on the disorientation angle may possibly result in different resistances to slip. Experimental data with a high value for k_2 yield a negative value for σ_0 when extrapolated to large grain sizes. Therefore, due to the changing grain boundary properties with increasing strain, k_2 should be a variable parameter and the use as a constant should be only considered as a coarse approximation for severely strained materials with smaller grain sizes [43].

Since hardness measurements are based on plastic deformation in the material, the above-described implications for flow stress should apply in a similar way to the hardness development in our samples and the LABs should provide an additional contribution to the hardness. Although the parameter of k_2 should be considered as variable for increasing strains, we tried to apply the alternative approach of Hansen [43]: As already used for the grain size comparison (Figure 4), the LABs are

included in the determination of d_{ND} (Figure 10b), resulting in a well-fitting linear regression for W_{pure} and W_K (except for W_K(4.6), which deviates by +500 MPa) and the Hall-Petch coefficient k_2^* (asterisk used as discrimination from Hall-Petch coefficient deduced from tensile tests). The fitting indicates that the CR process introduces a change in the grain boundary population by increasing the amount of dislocation boundaries with lower disorientation boundaries as shown by Hansen [43]. On the other hand, the observation, that the obtained linear regression for the Hall Petch relation applies well for the WR process when including only HABs, shows that the strength contribution of dislocation boundaries is constant for all WR samples (nevertheless different between W_K and W_{pure}). This is in line with the observed constant or even slightly decreasing LAB density during WR and the sudden increase in LAB density during CR (Figure 6).

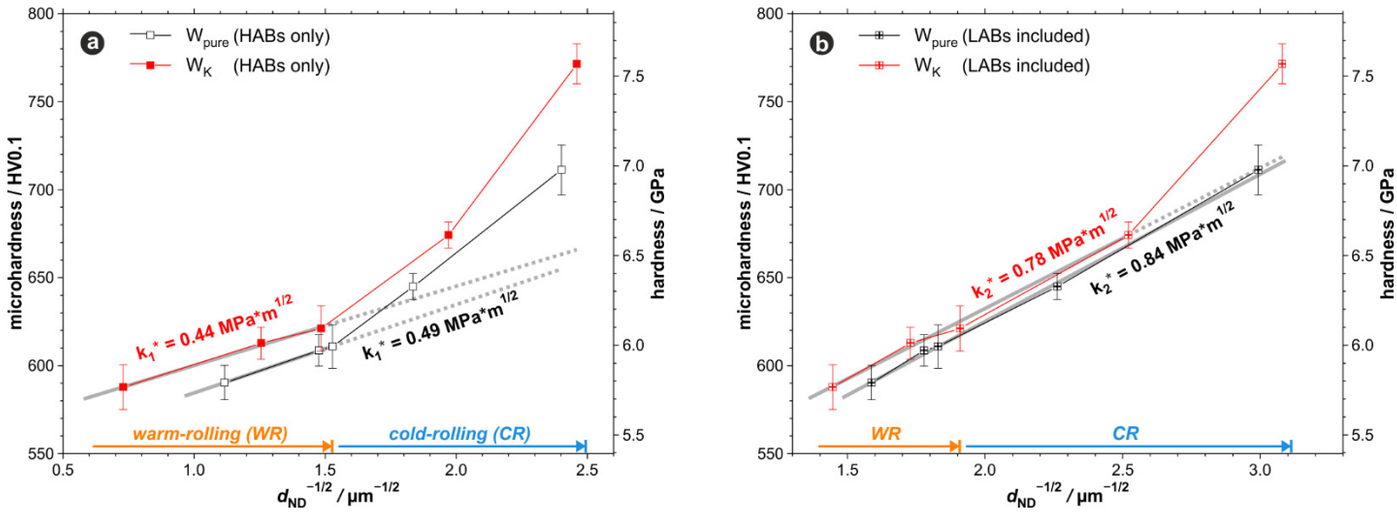

Figure 10. Vickers microhardness on grain size in normal direction (d_{ND}). (a) Only HABs are considered as grain boundaries. The linear regression (grey) is applied for the warm-rolled regime only and the fitted Hall-Petch coefficient k_1^* is given. The dotted line shows an extrapolation in the CR regime. (b) As an alternative approach, HABs and LABs are both included in the boundary spacing d_{ND}. The linear regression (grey) is applied for the whole rolling process (except for the last rolling step of W_K with large divergence) and the fitted coefficient k_2^* is given.

The observation in the difference of strength contribution of dislocation boundaries between both materials is seen in the generally higher base hardness of W_K compared to W_{pure} by a nearly constant ΔHV around 50-100 MPa when considering HABs and LABs in d_{ND} (Figure 10b). When only HABs are considered in in d_{ND}, the difference amounts to even ~150 MPa (Figure 10a). This slight difference between W_{pure} and W_K describes another contribution to the hardness beside the grain size effect and could be explained by three effects: (a) Precipitation hardening by aluminosilicates, which are forming during the sintering process [53,54]. Although most of Al and Si is removed from W_K by diffusion, the chemical analysis (Table 4) shows that these elements are partially retained, potentially still as aluminosilicates. Regarding the low content of 18 ppm Al and 5 ppm Si (Table 4), the contribution to the hardness should be minor. (b) Solid solution hardening by interstitial atoms like Al and Si [53]. As these elements are removed by diffusion, a fraction may be retained interstitially dissolved in the W lattice. Due to the low content of these elements, this hardening effect should be correspondingly rather limited. (c) Dislocations and dislocation networks interacting with K-bubbles. This could lead to an increased storage of dislocations and hence an increased work-hardening compared to W_{pure}. All three effects should combine additively and lead to a higher hardness of W_K compared to W_{pure} at the same grain size.

In conclusion, the development of hardness during deformation is influenced by formation of HABs, but LABs as well (especially during CR). K-doping itself also leads to a slightly higher hardness at comparable grain sizes.

4.2 TEM investigations

4.2.1 Dislocation and pore analysis

To investigate the mentioned influences on hardness, we performed a qualitative dislocation analysis by STEM imaging. The three thinnest K-doped sheets of $W_K(3.1)$, $W_K(3.7)$ and $W_K(4.6)$ were prepared by electrochemical thinning. Additional imaging results of an exemplary K-doped W sheet out of PLANSEE SE serial production have been included as well which serves as reference material for the present investigations. The specimen were prepared in such manner, that the viewing direction is parallel to normal direction.

In the comparison in Figure 11, $W_K(3.1)$ has the lowest degree of deformation and represents a sample where warm-rolling was the last rolling step. TEM imaging reveals an irregular grain shape. A low amount of grain boundaries is straight parallel to the rolling direction (Figure 11a, upper part of the image). Numerous dislocations can be seen in the grains, often aggregated, forming dislocation walls (Figure 11b). Nevertheless, the grain interior shows many regions completely free of dislocations.

The sample $W_K(3.7)$ represents the condition after the first cold-rolling step. The most apparent feature seen in the TEM images (Figure 11c, d) is the more elongated grain shape, arranged like interlocked roof tiles. Because of the interlocked arrangement, the length of the grains cannot be estimated. Due to different orientations, a high amount of inclined grain boundaries and a high dislocation density, only a few individual grains are translucent for the electron beam, depending on the sample tilt angle. Straight grain boundaries, parallel to the rolling direction, are much more common and the apparent dislocation density in the grain interior is increasing in comparison with the grain interior of $W_K(3.1)$. These dislocations are often arranged in X-shaped junctions, a common feature also observed in preliminary TEM-studies on 200 µm thick, K-doped W sheets by PLANSEE SE (standard product from serial production, labelled here as exemplary sheets) seen in Figure 12. Another feature, regularly found in the TEM images of $W_K(3.7)$ samples (also for $W_K(3.1)$ samples), are dislocation loops with diameters around <5 to 50 nm, which are often aligned in rows (Figure 11d, red frame). These rows (or so-called *debris*), can be left behind by moving dislocations as a direct result of intermediate sized edge jogs on screw dislocations. Such loops can form by diffusion and coalescence of vacancies (only at higher temperatures) and interstitials as well, or by interaction of dislocations on parallel slip planes [53]. The high probability of crossing dislocations on nonparallel slip planes is also given by the high amount of forest dislocations, leading to X-shaped junctions. This feature, which is commonly observed in the sample, will be discussed in the next section.

For $W_K(4.6)$, the width of the elongated grains decreases and a higher density of grain boundaries is observed, most of them aligned parallel to the RD (Figure 11e). The apparent amount of dislocations per volume increases significantly and the dislocations are densely packed in many areas (Figure 11f). Also dislocation loops are more common, albeit more irregularly distributed compared to the straight rows observed in $W_K(3.1)$ and $W_K(3.7)$.

Although estimations about the apparent dislocation density have to be taken with caution when TEM samples with unknown thicknesses are evaluated (approximately between 50 to 150 nm), the observed dislocation distribution is representative for the whole investigated sample volume. With increasing strain, a general trend to higher dislocation densities and a higher density of grain boundaries, especially straight boundaries parallel to the rolling direction, can be acknowledged. This shows that not only a grain size reduction along ND occurs, but also along TD, notably in the cold-rolled samples. The change in the microstructure and the dislocation density could be attributed to the increasing strain. On the other hand, since studies on screw dislocation glide in W show a change in the dislocation glide motion from classical straight to a more jerky motion beginning below 300 °C ([55] and references therein), and since this temperature regime is approached by the CR process, the change in microstructure and dislocation density could also indicate a change in the deformation mechanism of tungsten as well.

Regarding the high amount of regions especially in $W_K(4.6)$, which are densely packed with dislocations, some of these regions can be considered as dislocation boundaries (compare to [42]). This is in line with the increase of LAB density observed by EBSD (Figure 6) and hardness (Figure 9). These dislocation boundaries should be able to act as barriers for dislocation movement and therefore be responsible for the hardening behaviour of the cold-rolled W sheets. This would be an explanation for the behaviour observed in Figure 10, where the inclusion of LABs is necessary to apply a Hall-Petch relation.

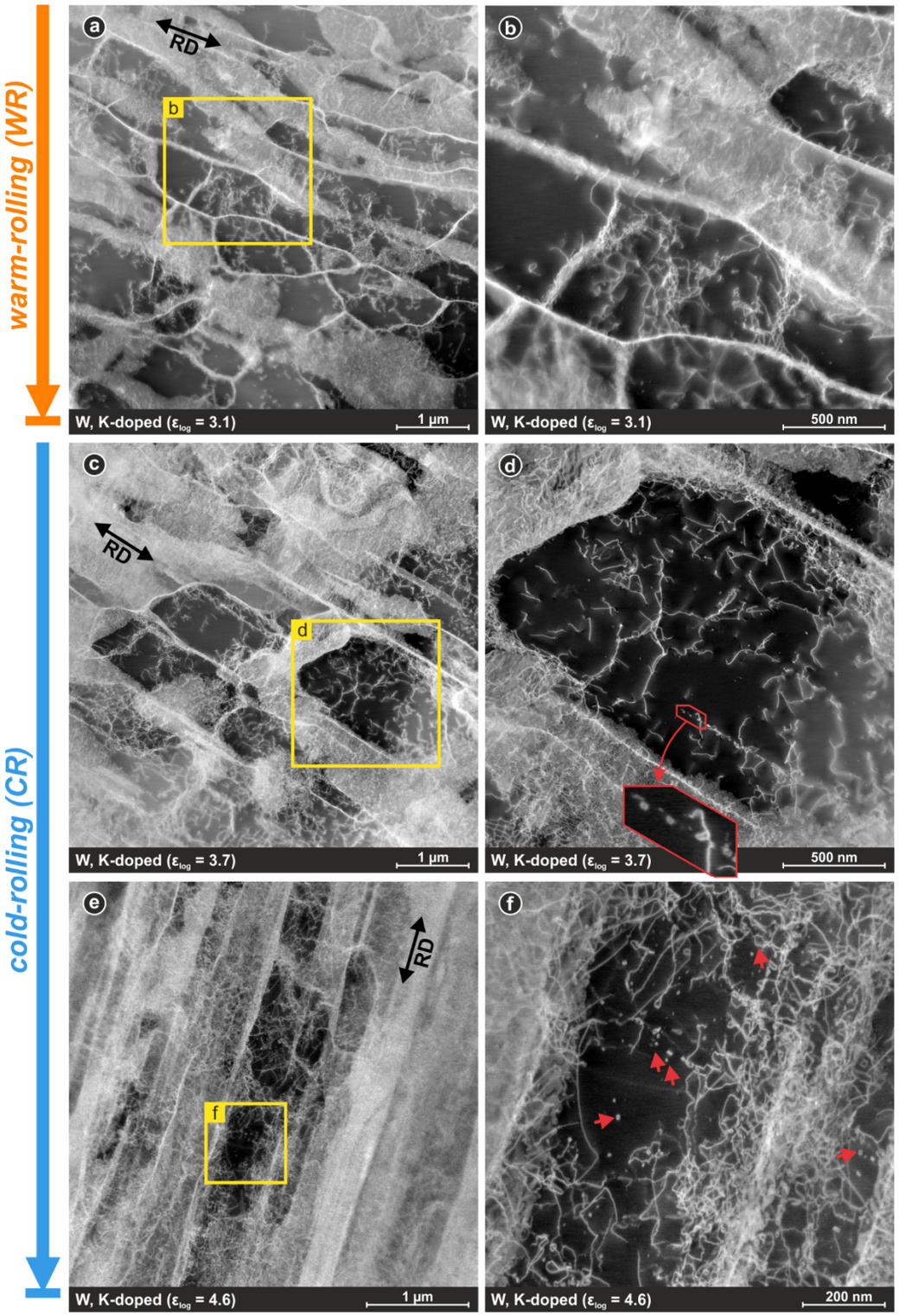

Figure 11. Comparison of dislocation structures between warm-rolled sample $W_K(3.1)$ (a, b) and both cold-rolled samples $W_K(3.7)$ (c, d) and $W_K(4.6)$ (e, f) as observed in TEM. All specimen are investigated by STEM imaging with normal direction (ND) as viewing direction. Respective overview on the left (a, c, e) with noted rolling direction (RD) and an enlarged detail marked by a yellow frame (b, d, f). Examples of observed dislocation loops marked by red arrows (f) or enlarged in red frame (d). Note the higher magnification for $W_K(4.6)$ (e, f) compared to the other samples.

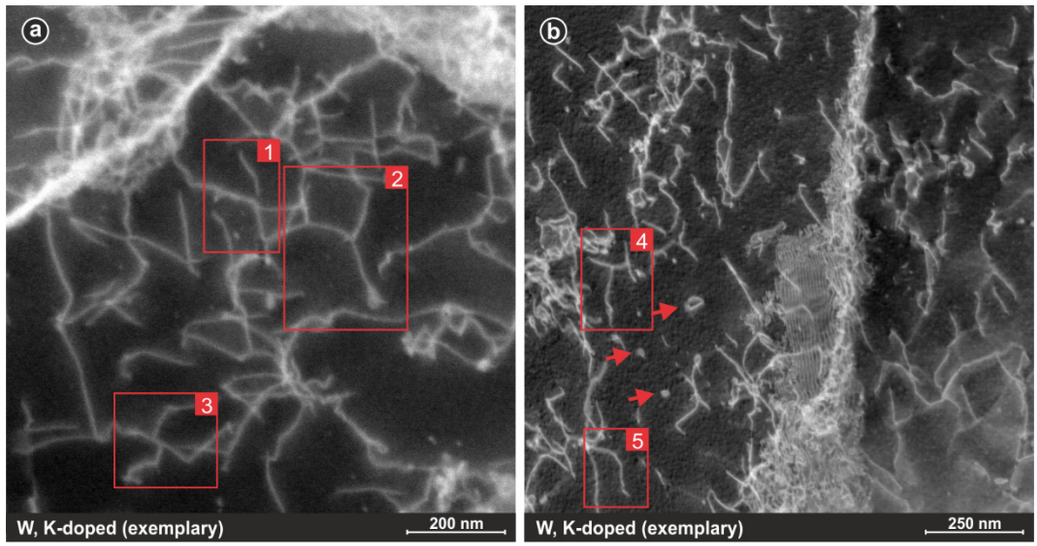

Figure 12. Overview of dislocation features observed in TEM samples of K-doped W sheets. Supposed X-shaped junctions are seen (marked by red frames 1-4), also a bulge (frame 5). Dislocation loops are marked by arrows (see also Figure 11d, f).

Another observable feature are pores or voids in the sample volume (often at grain boundaries), which are supposed to be K-bubbles (Figure 13). Such pores are not very common in the investigated samples of W_K and the sheet from serial production. That observation and the large pore volume (up to 500 nm) fits to the circumstance that we investigated the sheet in as-rolled condition and not in annealed condition. We suspect that during annealing a break-up of the bubbles into rows of smaller bubbles will occur and dispersion will improve, as known from K-doped tungsten wires [26,29]. The pores are mostly decorated with surrounding dislocations. This accumulation of dislocations gives an indication for a slight potential hardening effect by dislocation-bubble interactions, also observed in Figure 10, where W_K reaches slightly higher hardness compared to W_{pure} at the same grain size d_{ND}.

EDX measurements reveal minor amounts of Al in the bubble (Figure 13d). K could not be observed. However, the observed bubbles with dimensions of up to 500 nm (along RD and TD) are possibly opened by the electrochemical preparation of the approx. 100 nm thin TEM sample. Therefore, an initial K filling of the observed pores could have been partially or even completely removed by the dissolved NaOH. Si, an element also involved in the sintering process, is not detectable in the EDX spectrum due to its hidden K_α-line very near to the dominating M_α-line of W.

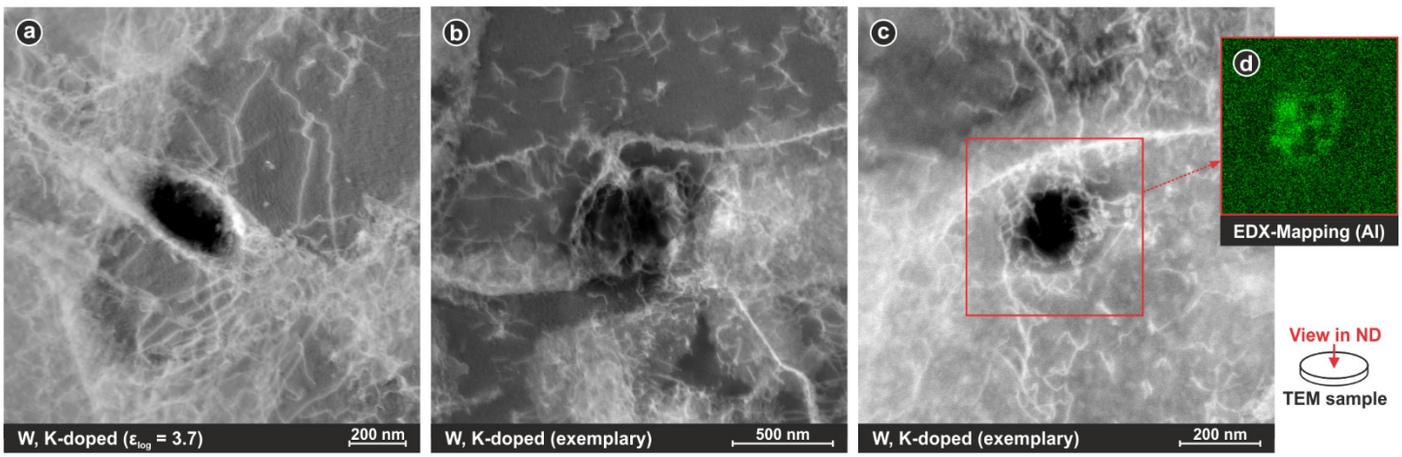

Figure 13. (a-c) Pores in K-doped W investigated by STEM imaging with ND as viewing direction. Around these supposed K-bubbles, an accumulation of dislocations can be observed, as well as a general tendency for the bubbles to be located near grain boundaries. (d) In some cases, EDX mapping reveals minor amounts of aluminium at the border of these pores, indicating that these might have been K-bubbles.

4.2.2 Modelling of dislocation interaction

Figure 12 shows some peculiar features of severely cold-rolled K-doped tungsten sheets: prismatic loops, bulges, and junctions. In order to improve our understanding of the hardening mechanisms as well as driving forces for recovery and recrystallization, we compare TEM images with results derived from simulations using the three-dimensional discrete dislocation dynamic (DDD) code by Weygand [39]. In the following, the modelling of the dynamic formation of two different types of junctions is described.

Under certain conditions, two gliding dislocations can attract (see Frank energy criterion [56], $(b_1 + b_2)^2 < b_1^2 + b_2^2$, or equivalently $b_1 b_2 < 0$) and merge into a product dislocation, a so called junction. This junction has a Burgers vector of $b_3 = b_1 + b_2$.

The first modelled example includes dislocation 1 with $b_1 = 1/2\,[1\bar{1}1]$ gliding on the $n_1 = (110)$ plane and dislocation 2 with $b_2 = 1/2\,[11\bar{1}]$ gliding on the $n_2 = (101)$ plane (Figure 14a). When the two dislocation lines collide, they form a junction along the $[1\bar{1}\bar{1}]$ intersection line of the planes and the junction segment has $b_3 = b_1 + b_2 = [100]$ (Figure 14a). The newly formed junction is immobile and can only zip and unzip (see also supplementary video 1). When the applied stress is sufficient to cause the junction to unzip, the dislocations will glide away. A more complex configuration can arise if another $1/2\,[\bar{1}11]$ dislocation reacts with the junction before it unzips ($[100] + 1/2\,[\bar{1}11] = 1/2\,[111]$). These configurations are referred to as multi-junctions and are very strong obstacles to dislocation motion [56].

The first modelled junction forms a segment along the $[1\bar{1}\bar{1}]$ intersection line of the $n_1 = (110)$ and $n_2 = (101)$ planes. However, Louchet and Kubin showed by TEM investigations on niobium single crystals, that under certain conditions, the junction can also be formed on a third plane, the cross-slip plane [57]. Therefore, in our second example, we modelled such a version of junction formation, which can be seen in the supplementary video 2. The video shows the following subsequent processes: Two Frank-Read sources are emitting dislocation loops. The first source operates in the $n_1 = (110)$ plane with $b_1 = 1/2\,[1\bar{1}1]$, the second one in the $n_2 = (\bar{1}10)$ plane with $b_2 = 1/2\,[11\bar{1}]$ (Figure 14b). Both sources are oriented such that the dislocation initially has a pure screw character (Burgers vector and line vector are parallel). The dislocation loops expand, attract and collide. Next, the first dislocation starts to cross slip on a third plane with $n_3 = (011)$. Afterwards, the second dislocation cross-slips on exactly the same plane. The moment of the second cross-slip event is the moment of the formation of a junction in the third plane, the cross-slip plane. The junction has $b_3 = b_1 + b_2 = [100]$ and is immobile, thus it can only zip and unzip.

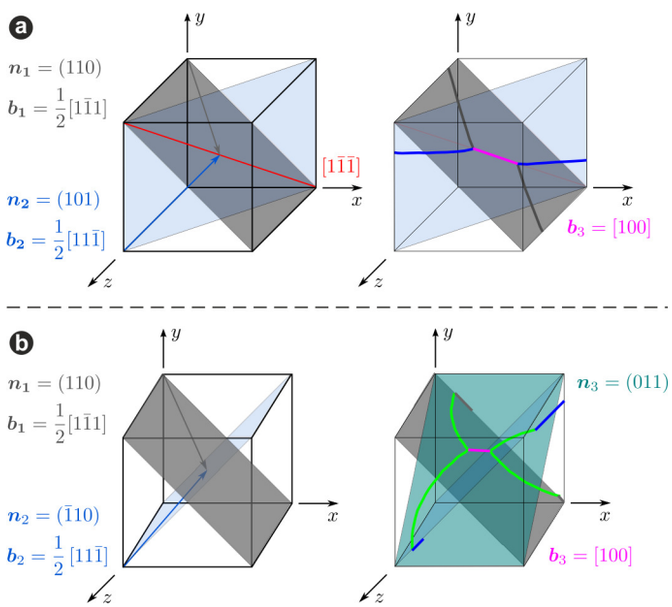

Figure 14. Dislocation junction formation modelled by discrete dislocation dynamics. Junctions are often-observed features in TEM images (Figure 12). In (a) the formation of a junction on two intersection planes is shown. In (b) the junction is formed on a third plane, the cross-slip plane. In each case the loading direction was in the y-direction. The formation of the two different junctions is visualised in the supplementary videos 1 and 2.

Ongoing TEM investigations should identify whether the first or second type of junction formation are more frequent in nature and how dislocation interaction can lead to an increase in the density of dislocation sources in the material. Since junctions are inhibiting the cross-slip of dislocations, the formation of junctions could be an opposing mechanism to recovery processes, where cross-slip is essential.

4.3 Annealed condition

4.3.1 Microhardness

A first indication of the microstructural evolution during isochronal annealing for 1 h is given by Vickers microhardness measurements (Figure 15). For pure W, a two-step process can be recognised with a first decrease in hardness ($\Delta HV_{step\ I}$) starting between 700 °C and 900 °C and a second severe decrease ($\Delta HV_{step\ II}$) between 1270 °C and 1400 °C (Figure 15, left). While the hardness loss in the first step is only minor for sheets with lowest strain ($\varepsilon_{\log}$ = 1.6) and resembles the hardness loss in other studies with similar strain [58], the loss is more severe for the other sheets with higher strain. This means that with increasing strain, $\Delta HV_{step\ I}$ increases as well. The initial increase in hardness for sheets with higher strain in as-rolled condition gets nearly completely lost after annealing at 900 °C for 1 h and the hardness of all sheets becomes similar in the range of 550 to 570 HV0.1 after annealing at this temperature. During annealing at higher temperatures up to 1270 °C, these values only slightly decrease further. After annealing above 1270 °C, the second step ($\Delta HV_{step\ II}$) is observed, where the hardness decreases below 450 HV0.1 near the hardness of a W single crystal at ~400 HV0.1 [3].

This two-step-process indicates two different restoration mechanisms and has been reported in another study with isothermal annealing of cold-rolled W sheets as well [59]. $\Delta HV_{step\ I}$ could be interpreted as recovery phenomenon. However, studies after annealing at 1027 °C (6 h) show a similar decrease in hardness in combination with an observed reduction of HAB density [12]. Since recovery processes only involve movement of LABs and rearrangement of dislocation networks without long range movement of HABs, the processes involving HABs, causing grain coarsening at low temperatures, have to be scrutinized. We suggest *extended recovery* (sometimes addressed as *continuous RX*) to be responsible. Continuous RX is described to occur only in highly deformed materials, provoked by a high HAB/LAB ratio [60,61]. The second step above 1270 °C, where the hardness becomes similar to the hardness of a single crystal, should be related to a discontinuous RX process by nucleation and migration of HAB [60–62], leading to a coarse grained microstructure.

The K-doped sheets reveal a similar two-step behaviour, although more complex (Figure 15, right). The first severe loss of hardness occurs likewise at 900 °C down to around 570 to 590 HV0.1, which is in a similar range as W_{pure}. For the sheet with the lowest strain, W_K(1.6), the onset temperature for the second step (with a drop below 450 HV0.1 as well) is also in the same range just above 1270 °C. However, sheets with higher strain show a different behaviour: W_K(2.7), W_K(3.1) and W_K(3.7) still maintain values of approximately 520 HV0.1 at 1400 °C and W_K(4.6) maintains 525 HV0.1 even at 1600 °C. The large error bar of W_K(4.6) at 1800 °C may be indicative for discontinuous RX, as growth of large recrystallized grains in the deformed matrix leads to a heterogeneous microstructure.

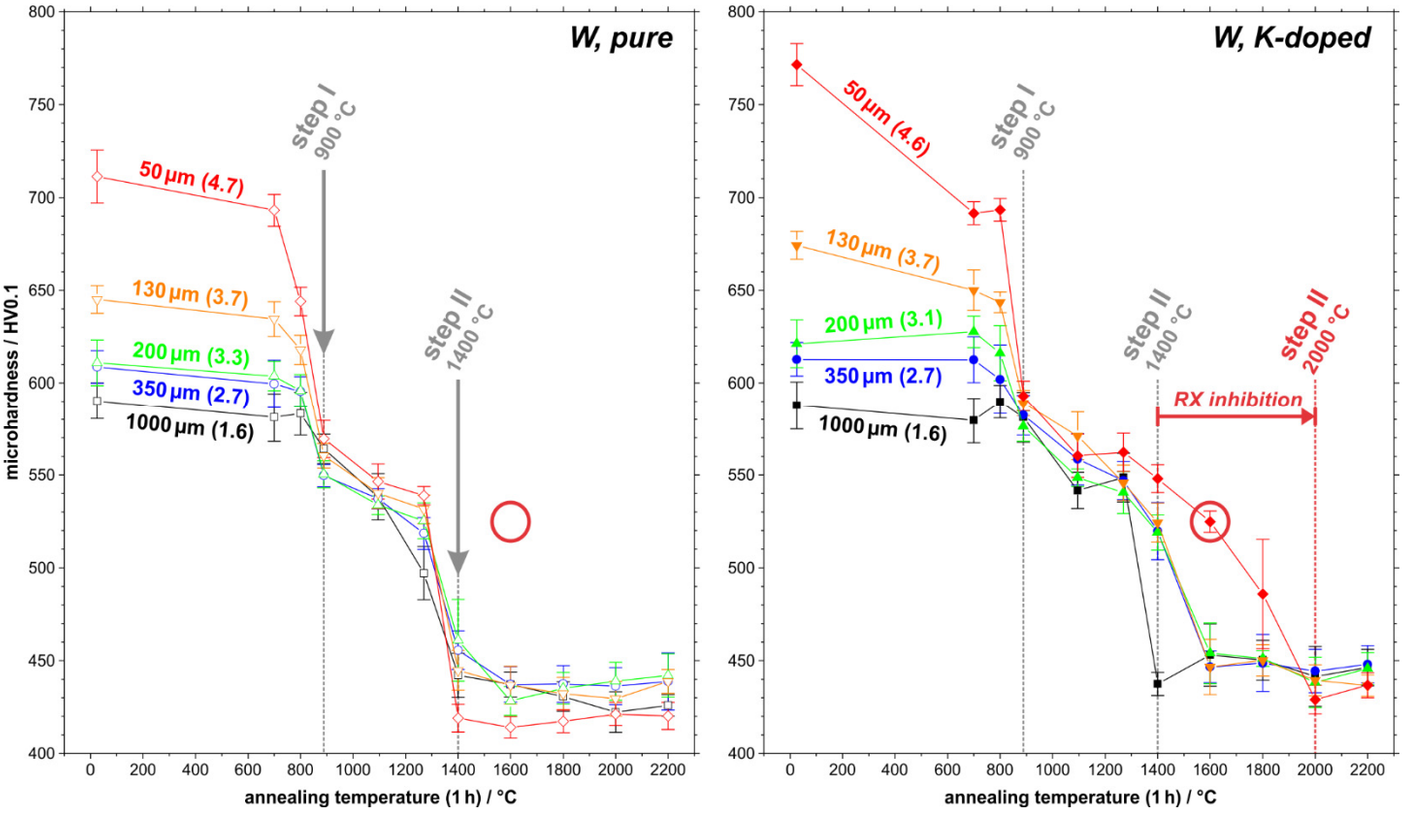

Figure 15. Microhardness values of pure W and K-doped W with different strain after annealing for 1 h in dependence on annealing temperature. Two restoration steps can be distinguished. Sheets with high degree of deformation show more pronounced restoration processes in the first stage. Red circle for reference between both materials at 1600 °C.

4.3.2 Microstructure

The shift of the second step in the hardness loss towards higher temperature for W_K indicates a stabilisation of its microstructure by the K-doping. An example for this stabilisation of the microstructure by K-doping can be seen in Figure 16 by BSE imaging. Samples of W_{pure}(3.7) and W_K(3.7) from the as-rolled condition (a, b) are compared to samples after annealing at 1400 °C for 2 h (c, d). W_{pure} shows significant larger grains and a rather homogenous microstructure (c). In contrary, a much finer microstructure is retained in the W_K sample (d). This behaviour is comparable to the two-step behaviour observed in the microhardness development (Figure 15), where at 1400 °C (1 h) W_K maintains mediocre hardness values after the first step, but W_{pure} already completed the second restoration step. Still, restoration has occurred for the K-doped material (Figure 16d), but obviously the progress of RX in the second step is inhibited. If the microstructure is investigated in more detail, a heterogeneous microstructure is observed with some larger, more equiaxed grains together with still elongated grains (Figure 16d, frame 2). This indicates that the second restoration step, which is inhibited by the K-doping, incorporates discontinuous RX or alternatively discontinuous RX and subsequent abnormal grain growth. More investigations are needed in order to identify the exact restoration mechanisms occurring during both steps.

Another common feature in the K-doped material are elongated pores in the as-rolled condition (Figure 16b, frame 1), where after annealing numerous rows of spherical pores occur, aligned like a pearl necklace (Figure 16d, frame 3). Since these are not observable in W_{pure}, we interpret them as K-bubbles. The break-up of K-bubbles, which is also known from K-doped W lamp wires and described by the Plateau-Rayleigh instability [23,28,29], seems to take place in our rolled W sheets during annealing at 1400 °C for 2 h as well, despite having theoretically much lower strains ($\varepsilon_{\log}$ = 3.7 in this sample) than usually achieved in wires. The critical aspect ratio needed for the break-up of the bubbles by the Rayleigh instability should be ≥ 8.89 [63]. However, the geometry of the bubbles in the as-rolled sheets should be more complicated than in drawn wires with one-dimensional elongation. Instead, a more flat, lath-like shape should be expected, which complicates applying for the break-up mechanism from the Rayleigh instability. Nevertheless, it is clearly shown that the break-up is active during annealing at least in our cold-rolled samples.

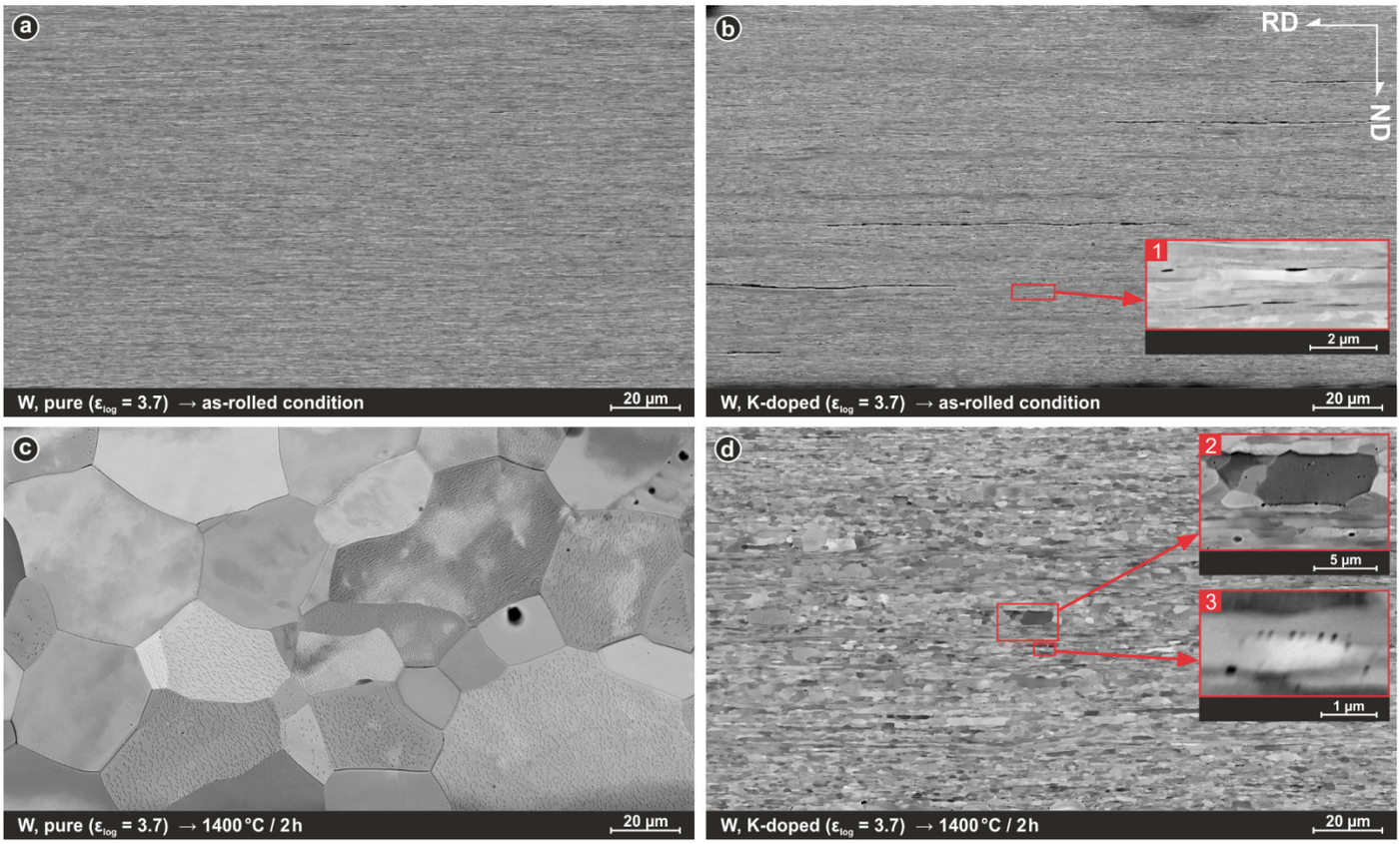

Figure 16. Comparison of pure (a, c) and K-doped (b, d) W samples (130 µm) in as-rolled condition and after annealing at 1400 °C for 2 h (BSE imaging in SEM on RD/ND sections). While pure tungsten shows growth of large recrystallized grains, K-doped tungsten still maintains smaller grain sizes. Enlarged areas show elongated K-bubbles by rolling (1), small recrystallized grains (2) and K-bubbles aligned in rows (3).

4.3.3 *Implications for K-doping effectiveness in RX inhibition*

Two important aspects can be highlighted: (1) Due to the similar restoration behaviour of W_K compared to W_{pure} up to 1270 °C, the K-doping seems to become effective at higher temperatures, indicating that only the second restoration step is affected. (2) The degree of deformation plays an important role for the effectiveness of RX inhibition by K-bubbles. Both aspects combined, it can be concluded that, despite the W_K sheet with highest strain has no benefit compared to the sheet with lowest strain at 900 °C due to higher loss of hardness, severe rolling of K-doped W sheets leads to an improved inhibition behaviour at temperatures above 1270 °C. This influence of the degree of deformation on the RX inhibition effectiveness of K-doping can be explained by the finer dispersion of K-bubbles: Further rolling leads to more elongated K-bubbles with higher aspect ratio, which break up into longer rows of smaller bubbles after annealing [23,28,29]. If we assume a pinning mechanism of grain boundaries similar to incoherent particles and apply the approximation of Zener and Smith [64,65] to describe the pinning force (or Zener pressure) P_Z of K-bubbles that are present in a sample volume, the relationship of the pinning force to the bubble radius r is reciprocal:

$$P_Z = -\frac{3}{2}\,\gamma\,\frac{f}{r} \tag{5}$$

with the grain boundary energy γ and the volume fraction of the bubbles f. Therefore, smaller bubbles should yield a higher Zener pressure and pin grain boundaries more effectively. A trend can be recognised, despite the fact that K-bubbles are often grouped in rows and the model should be used for a random particle distribution.

If the effectiveness of boundary pinning only increases with bubble break-up, this raises the question at which temperature the bubble break-up occurs and if that is the reason for the low effectiveness in the first restoration step (high $\Delta HV_{step\ I}$). Another reason could be the continuous RX mechanism itself. Continuous RX implies very local grain boundary movement and is therefore a recovery mechanism. Such local boundary movements should occur especially between the distributed

K-bubbles, where the grain boundary movement is unhindered. This would mean that an increased dispersion of K-bubbles not only along RD by bubble break-up, but also along ND (and TD) would be beneficial. Since the rolling process should theoretically only influence the dispersion along RD (and to a minor amount along TD) by elongation, an increased dispersion already during the sintering process should improve the general dispersion in the final product. Another obvious improvement of the restoration inhibition could be reached by increasing the total amount of K in W, although yet the complex process of AKS-doping sets a certain limitation to the maximum content of dopant elements.

5 Conclusions

In this study, we compared K-doped W sheets with five different rolling reductions to correspondingly rolled pure W sheets. The performed rolling scheme included warm-rolling and also subsequent cold-rolling for the two highest rolling reduction conditions. The results are summarized with respect to the initially posed main questions.

1) Differences in the rolling induced evolution of the microstructure of K-doped and pure tungsten have been assessed. K-doped and pure W show a similar evolution of the microstructure with ongoing grain size reduction down to mean grain sizes of below 180 nm. No signs of saturation of grain size reduction is observed, indicating that the grain size reduction could theoretically be continued by further rolling. While the HAB density is growing during warm-rolling, the LAB density remains constant, but increases significantly by cold-rolling, indicating that restoration processes take place during warm-rolling between 800 °C and 1000 °C. Also a drastic increase in hardness has been observed after cold-rolling, which increases more than expected by a Hall-Petch relation from warm-rolling, when only HABs (>15°) are considered. However, a linear relation can be applied with sufficient fitting, when additionally LABs are included, with a sole exception for the K-doped W with highest strain. By this relation, we described the dependence of hardness development on formation of HABs during warm-rolling. During cold-rolling a hardness contribution of LABs becomes important. The increased amount of dislocation boundaries in cold rolled samples is confirmed by TEM investigations.

We have shown that continuing the cold-rolling process to even higher degree of deformation than in previous studies [5,8] has the potential to increase its already excellent hardness properties. Further assessment of critical mechanical properties by fracture toughness and tensile tests will be necessary to characterize both materials in depth. Knowing the as-rolled condition of both materials in detail, the produced W sheets are suited for further studies of the recrystallization behaviour. This has been initiated by isochronal annealing and hardness measurements presented here.

2) TEM investigations in the doped material show up to 500 nm large voids in the rolling plane, decorated with dislocations. These are interpreted as former K-bubbles. Since we investigated the as-rolled condition, a break-up of large bubbles did not occur and we expect a much finer bubble distribution after annealing. Hence, an interesting point for next studies are investigations on the temperatures at which the break-up occurs.

3) Dislocation features have been investigated by TEM imaging, showing higher dislocation densities with increasing strain and an increasing amount of dislocation loops. We also observed dislocation junctions and their formation has been modelled by a three-dimensional discrete dislocation dynamic code. The simulations show that there are two distinct paths to the formation of those junctions.

4) The recrystallization behaviour after heat treatment has been evaluated by microhardness measurements. Both materials show a decrease in hardness beginning at 800 °C and the loss of hardness is increasing with increasing strain, resulting in nearly the same hardness for all rolled sheets after annealing for 1 h at 900 °C. We suppose that with increasing strain extended recovery (also addressed as continuous recrystallization) becomes the dominating restoration mechanism here.

For pure W, a second severe decrease in hardness to nearly the hardness of a W single crystal can be observed for all sheets above 1270 °C. For K-doped W, this decrease occurs at higher temperatures with increasing strain. The sheet with highest strain has the same hardness at 1600 °C as the pure W sheets at 1270 °C. A first microscopic comparison after annealing at 1400 °C for 2 h shows that growth of large grains is suppressed compared to pure W. The break-up process of K-bubbles known from lamp wires is also active in our W sheets, as shown after annealing. Altogether, this indicates that (1) the K-bubbles only effectively prevent growth of large grains at higher temperatures and (2) become more effective in recrystallization inhibition with higher degree of deformation due to increased distribution by bubble break-up. Further

investigations are required, to distinguish between the occurrence of discontinuous RX only and possible subsequent abnormal grain growth.

Despite K-doped tungsten wires are used for more than 100 years as incandescent lamp wires and many research has been done for the high temperature behaviour of the inherent bubbles, we only have minor understanding of the behaviour of K-bubbles in rolled sheets. Therefore, further studies of K-doped W sheets are needed, to understand the restoration mechanisms of the cold-rolled tungsten sheets in detail and to evaluate how the potential of K-bubbles as RX inhibitor can be improved.

Acknowledgements

This work has been carried out within the framework of the EUROfusion Consortium and has received funding from the Euratom research and training programme 2014-2018 and 2019-2020 under grant agreement No 633053. The views and opinions expressed herein do not necessarily reflect those of the European Commission. The support of the tungsten supplier, PLANSEE SE (Reutte/Austria), is gratefully acknowledged. We are thankful for chemical analysis by the group of Thomas Bergfeldt (IAM-AWP).

References

[1] M. Rieth, S.L. Dudarev, S.M. Gonzalez de Vicente, J. Aktaa, T. Ahlgren, S. Antusch, D.E.J. Armstrong, M. Balden, N. Baluc, M.-F. Barthe, W.W. Basuki, M. Battabyal, C.S. Becquart, D. Blagoeva, H. Boldyryeva, J. Brinkmann, M. Celino, L. Ciupinski, J.B. Correia, A. De Backer, C. Domain, E. Gaganidze, C. García-Rosales, J. Gibson, M.R. Gilbert, S. Giusepponi, B. Gludovatz, H. Greuner, K. Heinola, T. Höschen, A. Hoffmann, N. Holstein, F. Koch, W. Krauss, H. Li, S. Lindig, J. Linke, C. Linsmeier, P. López-Ruiz, H. Maier, J. Matejicek, T.P. Mishra, M. Muhammed, A. Muñoz, M. Muzyk, K. Nordlund, D. Nguyen-Manh, J. Opschoor, N. Ordás, T. Palacios, G. Pintsuk, R. Pippan, J. Reiser, J. Riesch, S.G. Roberts, L. Romaner, M. Rosiński, M. Sanchez, W. Schulmeyer, H. Traxler, A. Ureña, J.G. van der Laan, L. Veleva, S. Wahlberg, M. Walter, T. Weber, T. Weitkamp, S. Wurster, M.A. Yar, J.H. You, A. Zivelonghi, Recent progress in research on tungsten materials for nuclear fusion applications in Europe, J. Nucl. Mater. 432 (2013) 482–500. doi:10.1016/j.jnucmat.2012.08.018.

[2] W. Martienssen, H. Warlimont, Springer handbook of condensed matter and materials data, Springer Science & Business Media, Heidelberg, 2006.

[3] E. Lassner, W.-D. Schubert, Tungsten - Properties, Chemistry, Technology of the Element, Alloys, and Chemical Compounds, Kluwer Academic, New York, 1999. doi:10.1007/978-1-4615-4907-9.

[4] Q. Wei, L.J. Kecskes, Effect of low-temperature rolling on the tensile behavior of commercially pure tungsten, Mater. Sci. Eng. A. 491 (2008) 62–69. doi:10.1016/j.msea.2008.01.013.

[5] S. Bonk, J. Reiser, J. Hoffmann, A. Hoffmann, Cold-rolled tungsten (W) plates and foils: Evolution of the microstructure, Int. J. Refract. Met. Hard Mater. 60 (2016). doi:10.1016/j.ijrmhm.2016.06.020.

[6] J. Reiser, J. Hoffmann, U. Jäntsch, M. Klimenkov, S. Bonk, C. Bonnekoh, A. Hoffmann, T. Mrotzek, M. Rieth, Ductilisation of tungsten (W): On the increase of strength AND room-temperature tensile ductility through cold-rolling, Int. J. Refract. Met. Hard Mater. 64 (2017) 261–278. doi:10.1016/j.ijrmhm.2016.10.018.

[7] V. Nikolic, S. Wurster, D. Firneis, R. Pippan, Improved fracture behavior and microstructural characterization of thin tungsten foils, Nucl. Mater. Energy. 9 (2016) 181–188. doi:10.1016/j.nme.2016.06.003.

[8] C. Bonnekoh, A. Hoffmann, J. Reiser, The brittle-to-ductile transition in cold-rolled tungsten: On the decrease of the brittle-to-ductile transition by 600 K to − 65 °C, Int. J. Refract. Met. Hard Mater. 71 (2018) 181–189. doi:10.1016/J.IJRMHM.2017.11.017.

[9] J. Reiser, L. Garrison, H. Greuner, J. Hoffmann, T. Weingärtner, U. Jäntsch, M. Klimenkov, P. Franke, S. Bonk, C. Bonnekoh, S. Sickinger, S. Baumgärtner, D. Bolich, M. Hoffmann, R. Ziegler, J. Konrad, J. Hohe, A. Hoffmann, T. Mrotzek, M. Seiss, M. Rieth, A. Möslang, Ductilisation of tungsten (W): Tungsten laminated composites, Int. J. Refract. Met. Hard Mater. (2017). doi:10.1016/j.ijrmhm.2017.07.013.

[10] A. Alfonso, D. Juul Jensen, G.-N. Luo, W. Pantleon, Recrystallization kinetics of warm-rolled tungsten in the temperature range 1150-1350 °C, J. Nucl. Mater. 455 (2014) 591–594. doi:10.1016/j.jnucmat.2014.08.037.

[11] A. Alfonso, D. Juul Jensen, G.-N. Luo, W. Pantleon, Thermal stability of a highly-deformed warm-rolled tungsten plate in the temperature range 1100-1250 °C, Fusion Eng. Des. 98–99 (2015) 1924–1928. doi:10.1016/j.fusengdes.2015.05.043.

[12] C. Bonnekoh, P. Lied, T. Karcher, H. Leiste, A. Hoffmann, J. Reiser, The brittle-to-ductile transition in cold-rolled tungsten plates: Blurred transition after stress relieving and the origin of 45° embrittlement, To Be Publ. (2019).

[13] S. Bonk, J. Hoffmann, A. Hoffmann, J. Reiser, Cold-rolled tungsten (W) plates and foils: Evolution of the tensile

properties and their indication towards deformation mechanisms, Int. J. Refract. Met. Hard Mater. 70 (2018) 124–133. doi:10.1016/J.IJRMHM.2017.09.007.
[14] J. Reiser, M. Rieth, A. Möslang, B. Dafferner, J. Hoffmann, T. Mrotzek, A. Hoffmann, D.E.J. Armstrong, X. Yi, Tungsten foil laminate for structural divertor applications – Joining of tungsten foils, J. Nucl. Mater. 436 (2013) 47–55. doi:10.1016/j.jnucmat.2013.01.295.
[15] J. Reiser, M. Rieth, A. Möslang, H. Greuner, D.E.J. Armstrong, T. Denk, T. Gräning, W. Hering, A. Hoffmann, J. Hoffmann, H. Leiste, T. Mrotzek, R. Pippan, W. Schulmeyer, T. Weingärtner, A. Zabernig, Tungsten (W) Laminate Pipes for Innovative High Temperature Energy Conversion Systems, Adv. Eng. Mater. 17 (2015) 491–501. doi:10.1002/adem.201400204.
[16] M. Rieth, J. Reiser, B. Dafferner, S. Baumgärtner, The impact of refractory material properties on the helium cooled divertor design, Fusion Sci. Technol. 61 (2012) 381–384. doi:10.13182/FST12-1T3.
[17] I. Wesemann, W. Spielmann, P. Heel, A. Hoffmann, Fracture strength and microstructure of ODS tungsten alloys, Int. J. Refract. Met. Hard Mater. 28 (2010) 687–691. doi:10.1016/j.ijrmhm.2010.05.009.
[18] G. Leichtfried, Molybdenum lanthanum oxide: Special material properties by dispersoid refining during deformation, Adv. Powder Metall. 9 (1992) 123–138.
[19] P. Jenuš, A. Iveković, M. Kocen, A. Šestan, S. Novak, W2C-reinforced tungsten prepared using different precursors, Ceram. Int. 45 (2019) 7995–7999. doi:https://doi.org/10.1016/j.ceramint.2018.11.187.
[20] H.W. Deng, Z.M. Xie, Y.K. Wang, R. Liu, T. Zhang, T. Hao, X.P. Wang, Q.F. Fang, C.S. Liu, Mechanical properties and thermal stability of pure W and W-0.5wt%ZrC alloy manufactured with the same technology, Mater. Sci. Eng. A. 715 (2018) 117–125. doi:https://doi.org/10.1016/j.msea.2017.12.112.
[21] S. Antusch, J. Reiser, J. Hoffmann, A. Onea, Refractory Materials for Energy Applications, Energy Technol. 5 (2017) 1064–1070. doi:10.1002/ente.201600571.
[22] P. Schade, H.M. Ortner, I. Smid, Refractory metals revolutionizing the lighting technology: A historical review, Int. J. Refract. Met. Hard Mater. 50 (2015) 23–30. doi:10.1016/J.IJRMHM.2014.11.002.
[23] P. Schade, 100years of doped tungsten wire, Int. J. Refract. Met. Hard Mater. 28 (2010) 648–660. doi:10.1016/j.ijrmhm.2010.05.003.
[24] E. Pink, L. Bartha, The metallurgy of doped/non-sag tungsten, Elsevier Applied Science, London, 1989.
[25] D.M. Moon, R. Stickler, Creep behavior of fine wires of powder-metallurgical pure, doped, and thoriated tungsten, (1971). https://www.osti.gov/servlets/purl/4644368.
[26] D.M. Moon, R.C. Koo, Mechanism and kinetics of bubble formation in doped tungsten, Metall. Mater. Trans. B. 2 (1971) 2115–2122. doi:10.1007/BF02917539.
[27] A. Hoffmann, I. Wesemann, Potassium-doped Tungsten: Beyond Incandescent Lamp Wires, Int. J. Powder Metall. 47 (2011) 10.
[28] C.L. Briant, Potassium bubbles in tungsten wire, Metall. Trans. A. 24 (1993) 1073–1084. doi:10.1007/BF02657238.
[29] P. Harmat, L. Bartha, T. Grósz, The rate of bubble deformation during tungsten wire drawing, Int. J. Refract. Met. Hard Mater. 20 (2002) 295–299. doi:10.1016/S0263-4368(02)00027-6.
[30] W.F. Freyland, F. Hensel, The Vapour Pressure Curve of Liquid Potassium up to the Critical Point, Berichte Der Bunsengesellschaft Für Phys. Chemie. 76 (1972) 16–19. doi:10.1002/BBPC.19720760106.
[31] M. Fukuda, S. Nogami, K. Yabuuchi, A. Hasegawa, T. Muroga, Anisotropy in the Mechanical Properties of Potassium and Rhenium Doped Tungsten Alloy Plates for Fusion Reactor Applications, Fusion Sci. Technol. 68 (2015) 690–693. doi:10.13182/fst14-998.
[32] M. Fukuda, T. Tabata, A. Hasegawa, S. Nogami, T. Muroga, Strain rate dependence of tensile properties of tungsten alloys for plasma-facing components in fusion reactors, Fusion Eng. Des. 109–111 (2016) 1674–1677. doi:10.1016/j.fusengdes.2015.10.032.
[33] K. Sasaki, K. Yabuuchi, S. Nogami, A. Hasegawa, Effects of temperature and strain rate on the tensile properties of potassium-doped tungsten, J. Nucl. Mater. 461 (2015) 357–364. doi:10.1016/j.jnucmat.2015.03.015.
[34] J. Neges, B. Ortner, G. Leichtfried, H.P. Stüwe, On the 45° embrittlement of tungsten sheets, Mater. Sci. Eng. A. 196 (1995) 129–133. doi:10.1016/0921-5093(94)09706-2.
[35] PLANSEE, Wolfram, (n.d.). https://www.plansee.com/de/werkstoffe/wolfram.html (accessed October 11, 2018).
[36] PLANSEE, WVM-Blech Produktspezifikation (PSE-605-PS-167 Rev. 00), n.d.
[37] G. Gottstein, Materialwissenschaft und Werkstofftechnik : Physikalische Grundlagen, Springer-Vieweg, Berlin-Heidelberg, 2014. doi:10.1007/978-3-642-36603-1 ISBN.
[38] DIN EN ISO 6507-1:2018-07, Metallic materials – Vickers hardness test – Part 1: Test method; German version, (2018).
[39] D. Weygand, L.H. Friedman, E. Van Der Giessen, A. Needleman, Aspects of boundary-value problem solutions with three-dimensional dislocation dynamics, Model. Simul. Mater. Sci. Eng. 10 (2002) 437–468. doi:10.1088/0965-0393/10/4/306.
[40] J. Gil Sevillano, P. van Houtte, E. Aernoudt, Large strain work hardening and textures, Prog. Mater. Sci. 25 (1980) 69–134. doi:10.1016/0079-6425(80)90001-8.
[41] C. Bonnekoh, U. Jäntsch, J. Hoffmann, H. Leiste, A. Hartmaier, D. Weygand, A. Hoffmann, J. Reiser, The brittle-to-

ductile transition in cold-rolled tungsten plates: Impact of crystallographic texture, grain size and dislocation density on the transition temperature, Int. J. Refract. Met. Hard Mater. 78 (2019) 146–163. doi:10.1016/J.IJRMHM.2018.09.010.
[42] N. Hansen, New Discoveries in Deformed Metals, 32 (2001) 2917–2935.
[43] N. Hansen, Hall–Petch relation and boundary strengthening, Scr. Mater. 51 (2004) 801–806. doi:10.1016/J.SCRIPTAMAT.2004.06.002.
[44] M.R. Barnett, J.J. Jonas, Influence of Ferrite Rolling Temperature on Microstructure and Texture in Deformed Low C and IF Steels., ISIJ Int. 37 (1997) 697–705. doi:10.2355/isijinternational.37.697.
[45] C. Zhang, Z. Liu, G. Wang, Effects of hot-rolled shear bands on formability and surface ridging of an ultra purified 21%Cr ferritic stainless steel, J. Mater. Process. Technol. 211 (2011) 1051–1059. doi:10.1016/J.JMATPROTEC.2011.01.005.
[46] U.F. Kocks, C.N. Tomé, H.-R. Wenk, Texture and anisotropy: preferred orientations in polycrystals and their effect on materials properties, Cambridge university press, 1998.
[47] J.J. Jonas, Transformation Textures Associated with Steel Processing, in: A. Haldar, S. Suwas, D. Bhattacharjee (Eds.), Microstruct. Texture Steels, Springer London, London, 2009: pp. 3–17. doi:10.1007/978-1-84882-454-6_1.
[48] M. Hölscher, D. Raabe, K. Lücke, Relationship between rolling textures and shear textures in f.c.c. and b.c.c. metals, Acta Metall. Mater. 42 (1994) 879–886. doi:10.1016/0956-7151(94)90283-6.
[49] R. Song, D. Ponge, D. Raabe, J.G. Speer, D.K. Matlock, Overview of processing, microstructure and mechanical properties of ultrafine grained bcc steels, Mater. Sci. Eng. A. 441 (2006) 1–17. doi:10.1016/J.MSEA.2006.08.095.
[50] E.O. Hall, The Deformation and Ageing of Mild Steel: III Discussion of Results, Proc. Phys. Soc. Sect. B. 64 (1951) 747–753. doi:10.1088/0370-1301/64/9/303.
[51] N.J. Petch, The Cleavage Strength of Polycrystals, J. Iron Steel Inst. (1953) 25–28.
[52] R. Armstrong, I. Codd, R.M. Douthwaite, N.J. Petch, The plastic deformation of polycrystalline aggregates, Philos. Mag. A J. Theor. Exp. Appl. Phys. 7 (1962) 45–58. doi:10.1080/14786436208201857.
[53] D. Hull, D.J. Bacon, Introduction to Dislocations (Fifth Edition), 5th ed., 2011. doi:http://dx.doi.org/10.1016/B978-0-08-096672-4.00019-0.
[54] W.-D. Schubert, B. Lux, B. Zeiler, Formation and Incorporation of Dopant Phases during Technical Reduction of NS-Doped Tungsten Blue Oxide, Chem. Non-Sag Tungsten. (1995) 119–135. doi:10.1016/B978-0-08-042676-1.50014-2.
[55] D. Caillard, Geometry and kinetics of glide of screw dislocations in tungsten between 95K and 573K, Acta Mater. 161 (2018) 21–34. doi:10.1016/j.actamat.2018.09.009.
[56] V. V. Bulatov, L.L. Hsiung, M. Tang, A. Arsenlis, M.C. Bartelt, W. Cai, J.N. Florando, M. Hiratani, M. Rhee, G. Hommes, T.G. Pierce, T.D. de la Rubia, Dislocation multi-junctions and strain hardening, Nature. 440 (2006) 1174–1178. doi:10.1038/nature04658.
[57] F. Louchet, L.P. Kubin, Dislocation substructures in the anomalous slip plane of single crystal niobium strained at 50 K, Acta Metall. 23 (1975) 17–21. doi:10.1016/0001-6160(75)90064-4.
[58] Y. Yuan, H. Greuner, B. Böswirth, K. Krieger, G.-N. Luo, H.Y. Xu, B.Q. Fu, M. Li, W. Liu, Recrystallization and grain growth behavior of rolled tungsten under VDE-like short pulse high heat flux loads, J. Nucl. Mater. (2013). doi:10.1016/j.jnucmat.2012.04.022.
[59] U.M. Ciucani, A. Thum, C. Devos, W. Pantleon, Isothermal annealing of thin rolled tungsten plates in the temperature range from 1300 °C to 1400 °C, Nucl. Mater. Energy. 15 (2018) 128–134. doi:10.1016/J.NME.2018.03.009.
[60] F.J. Humphreys, M. Hatherly, Recrystallization and Related Annealing Phenomena, Elsevier, 2004. doi:10.1016/B978-0-08-044164-1.X5000-2.
[61] H. Jazaeri, F.J. Humphreys, The transition from discontinuous to continuous recrystallization in some aluminium alloys: II – annealing behaviour, Acta Mater. 52 (2004) 3251–3262. doi:10.1016/J.ACTAMAT.2004.03.031.
[62] D. Raabe, Recovery and Recrystallization: Phenomena, Physics, Models, Simulation, in: Phys. Metall., 2014: pp. 2291–2397. doi:10.1016/B978-0-444-53770-6.00023-X.
[63] P. Schade, Bubble evolution and effects during tungsten processing, Int. J. Refract. Met. Hard Mater. 20 (2002) 301–309. doi:10.1016/S0263-4368(02)00061-6.
[64] C.S. Smith, Zener pinning, Trans. Met. Soc. AIME. 175 (1948) 15–51.
[65] P.A. Manohar, M. Ferry, T. Chandra, Five Decades of the Zener Equation., ISIJ Int. 38 (1998) 913–924. doi:10.2355/isijinternational.38.913.